

**Outflows of very ionized gas in the center of Seyfert galaxies:
kinematics and physical conditions¹**

Alberto Rodríguez-Ardila

*Laboratório Nacional de Astrofísica/MCT, Rua dos Estados Unidos 154, CEP 37504-364,
Itajubá, MG, Brazil*

aardila@lna.br

M. Almudena Prieto

*Instituto de Astrofísica de Canarias, Tenerife, Spain & Max-Planck Institute for Astronomy,
Heidelberg, Germany*

and

Sueli Viegas and Ruth Gruenwald

Instituto de Astronomia, Geofísica e Ciências Atmosféricas - USP, Brazil

ABSTRACT

Medium resolution spectra (100 km s^{-1}) are used to deduce the size and kinematics of the coronal lines in a sample of nearby Seyfert galaxies (Circinus, NGC 1386, NGC 1068, NGC 3227, NGC 3783 and MCG-6-30-15) by means of simultaneous observations of [Fe XI] 7889 Å, [Fe X] 6374 Å, [Fe VII] 6087 Å, [Si VI] 2.48 μm and [Si VII] 1.96 μm . The coronal lines extend from the unresolved nucleus up to distances between a few tens to a few hundreds of parsecs. The region of the highest ionized ions studied, [Fe XI] and [Fe X], is the least spatially extended, and concentrates at the center; intermediate ionization lines extend from the nucleus up to a few tens to a few hundred parsecs; lower [O III]-like ions are known to extend in the kpc range. All together indicates a stratification in the ionized gas, usually interpreted in terms of nuclear photoionization as the driving ionization mechanism. However, coronal line profiles show various peculiarities: they are broader by a factor of two than lower ionization lines, the broadening being in terms of asymmetric blue wings, and their centroid position at the nucleus is blueshifted by a few hundreds of km s^{-1} . Moreover, in two objects –NGC 1386 and NGC 1068, a double peak [Fe VII] 6087 Å line is detected in the nuclear

¹Based on observations made with ESO Telescopes at the Paranal Observatory under programme ID 68.B-0627

and extended coronal region, this being the first report in the literature of such type of profile in coronal lines in active galactic nuclei. If interpreted as outflow signatures, the total broadening of the lines at zero intensity levels implies gas velocities up to 2000 km s^{-1} . Although the stratification of ions across the coronal region means that photoionization is the main power mechanism, the high velocities deduced from the line profiles, the relatively large spatial extension of the emission, and the results from single cloud photoionization models indicate that an additional mechanism is at work. We suggest that shocks generated by the outflow could provide the additional required power for line formation.

Subject headings: galaxies: Seyfert - line: formation - infrared: galaxies galaxies: individual(NGC 1068, Circinus, NGC 3783, MGC-6-30-15, NGC 1386, NGC 3227)

1. Introduction

Coronal lines (CL) are collisionally excited forbidden transitions within low-lying levels of highly ionized species (ionization potential $> 100 \text{ eV}$). They can be produced by either a hard UV continuum (Ferguson et al. 1997), a hot collisionally ionized plasma (Viegas-Aldrovandi & Contini 1989) or most plausible, a mix of both processes (Contini et al. 1998a). Because of their high ionization potential (IP), these lines are particularly suitable for getting information on the otherwise difficult to access observationally, extreme UV - soft X-ray region of the ionizing spectrum (Prieto & Viegas 2000). Due to the high energies involved in their production, coronal lines are genuine tracers of the AGN power mechanism. Pure starbursts when boosted by massive O-B stars in their Wolf-Rayet phase, may show He II lines but not lines of higher ionization potential ions ($\chi > 54 \text{ eV}$).

Observationally, coronal lines are present with comparable strength in AGN spectra regardless of their class (Penston et al. 1984; Erkens et al. 1997; Prieto & Viegas 2000; Rodríguez-Ardila et al. 2002; Reunanen et al. 2003). The peak position is usually blueshifted relative to the systemic velocity of the host galaxy ($\Delta V \sim 500\text{-}800 \text{ km s}^{-1}$) and broader than low ionization lines (Penston et al. 1984; De Robertis & Osterbrock 1986; Erkens et al. 1997; Rodríguez-Ardila et al. 2002). That has led to the idea that CL are associated with outflows, formed in an intermediate region between the classical narrow-line- and broad-line-region (NLR and BLR, respectively). The broad line region has sizes of less than a few hundred light-days (Peterson et al. 2004) and thus remains unresolved; the coronal region because of its lower velocity dispersion should be placed further out but still relatively close to the BLR, considering the high ionization level of the gas. Accordingly, the coronal region has also remained spatially unresolved.

The physical nature of the CLR has called the attention of many authors starting by the pioneer work by Penston et al. (1984), who discover the systematic blueshifting and broadening of this high ionization gas. Erkens et al. (1997) found that the CL occurs predominantly in objects

with a soft X-ray excess and suggest a possible relationship between the CLR and the absorption edges associated with warm absorbers present in nearly 50% of AGN. Porquet et al. (1999) showed that the CL may, in fact, be formed by the warm absorber. If that is the case, the CLR should be dense ($n \sim 10^6 \text{ cm}^{-3}$) and located at comparable distance as the broad line region. On the other hand, Ferguson et al. (1997) photoionization calculations show that the CLR can form in gas with densities of $10^2 - 10^{8.5} \text{ cm}^{-3}$ and extends up to several hundred parsecs, thus coinciding with the size of the extended NLR. However, they claim that except for the lower ionization coronal lines ([Ne v], [Si vii], [Ca viii] and [Fe vii]) that can form efficiently in gas that is roughly ~ 10 pc and beyond, the rest of coronal lines form optimally in gas that is less than 10 pc from the ionization source.

Coronal lines are present all across the electromagnetic spectrum. The highest ionization species are located in the X-rays region. In the optical, the most prominent ones are from iron. Dust extinction and the fact that reliable detection of these lines requires medium to high spectral resolution and large S/N ratios has made measurements of these lines difficult. The near- and mid-infrared regions, less affected by extinction, are very rich in coronal lines from different species and ionization levels. Indeed, they are often the dominant lines in the near-IR spectra of Seyfert galaxies (Reunanen et al. 2003).

The current availability of adaptive optics in 8 m telescopes enabled Prieto et al. (2005) to determine the size and morphology of the coronal line region for the first time. That is found to extend from the nucleus up to 30 to 200 pc radii at most, and be aligned preferentially with the direction of the lower-ionization cones seen in Seyfert galaxies. As expected, the coronal line region (CLR) is primarily produced very close to the active nucleus but is nevertheless resolved over several tens of parsecs. This, together with its preferential alignment with the ionization cone prompts to the possibility that the nuclear radiation is intrinsically collimated or that some additional in-situ excitation mechanism is needed to explain CL gas at those observed distances from the ionizing source. This paper attempts to address those issues by studying the physical conditions of the coronal line gas and its kinematics.

To that aim, we present high-sensitive observations with spectral resolution $R \sim 100 \text{ km s}^{-1}$ of Fe and Si coronal lines located in the visible and near-infrared spectra respectively. As stated above, the goal is determining the kinematics of the emitting region and constraining the physical properties of the coronal gas. To that aim, a sample of six nearby AGN were selected, and spectra centered at the position of a selected group of bright coronal lines are studied. In the optical, we selected [Fe vii] 6087 Å (IP=100 eV), [Fe x] 6374 Å (IP=240 eV) and [Fe xi] 7889 Å (IP=260e V). In the near-IR, [Si vi] 1.963 μm (IP=170 eV) and [Si vii] 2.48 μm (IP=205 eV) were chosen. These lines are all located near in wavelength to low-ionization lines, easing the comparison regarding the size of the emitting region and the shape of the line profiles between different ionization levels. In § 2, we describe the sample, the observations and data reduction process. The determination of the coronal region size based on the available data is carried out in § 3. In § 4 we discuss and compare the size of the CLR with that determined for the NLR using our data and the literature.

A comparison of the observed emission line profiles to unravel the kinematics of the coronal gas is in § 5. Photoionization and shock models to explain the physical conditions of the coronal gas are described in § 6. An overview of our main results and conclusions are in § 7.

2. Observations

In order to maximize the spatial resolution in physical scales, the sample of objects chosen for this work is composed of six of the nearest and brightest Seyfert galaxies: Circinus (Seyfert 2), NGC 1068 (Seyfert 2), NGC 1386 (Seyfert 2), NGC 3783 (Seyfert 1), MCG-6-30-15 (Seyfert 1) and NGC 3227 (Seyfert 1.5). Table 1 lists the characteristics of these galaxies. The spatial scale (pc/”) was derived assuming $H_0=75 \text{ km s}^{-1} \text{ Mpc}^{-1}$. These objects were observed at medium resolution spectroscopy, $R=2600$ ($\sim 120 \text{ km s}^{-1}$) in the optical, $R=3000$ ($\sim 100 \text{ km s}^{-1}$) in the near-IR, with a slit width= $1''$, the slit being always oriented north-south. The slit was nearly aligned to the PA of the [O III] emission for most sources, listed in column 5 of Table 1. The differences in position angle of the extended ionized gas and that of the slit is, for the majority of sources, not larger than 15° , except for MCG-6-30-15, where the difference is 65° and the opening angle is small, about 30° maximum. In Circinus, the slit is aligned with the edge of the ionization cone: the PA of the cone is -44° NW but the opening angle of the cone is $\sim 90^\circ$.

The spectroscopic configurations, telescopes and instrumentation employed for the optical and near-infrared observations as well as data reduction and extraction procedures were as follows. Log of the observations is in Table 2.

The optical iron coronal lines [Fe VII], [Fe X] and [Fe XI] were observed, in service mode (program 68.B-0627(A)), with the imaging-spectrograph EMMI at the ESO/NTT. Two grating positions were needed: one centered at $\lambda=6230 \text{ \AA}$, in order to include the [Fe VII] and [Fe X] lines and the low-ionization line [O I] $\lambda 6300 \text{ \AA}$, used for comparative purposes. The plate scale of this setup is $0.35''/\text{pix}$. The second position was centered at $\lambda=7950 \text{ \AA}$ to observe the [Fe XI] $\lambda 7890 \text{ \AA}$ line (plate scale $0.27''/\text{pix}$).

Data were reduced using *IRAF* standard procedures, that is, bias subtraction and division by a flat field frame. Wavelength and flux calibration were carried out by means of HeNeAr lamp frames and observations of spectroscopic standards taken during the night, respectively. A log of observations is presented in Table 2. 1-D frames were extracted from the 2-D images by summing up rows along the spatial direction. The optimal number of rows to be summed varied from source to source and depended on the achieved spatial resolution.

For the near-IR coronal lines, the observations were carried out also in service mode (program 68.B-0627(B)) with the imager-spectrograph ISAAC mounted on the VLT/ANTU 8.2m telescope. Two different grating positions were used. For the spectral region covering [Si VI] 19630 \AA , the grating was centered at $\lambda=19800 \text{ \AA}$. This setup allows the simultaneous observation of that line and H_2 19570 \AA . The second grating position, centered at 24400 \AA , was to observe [Si VII] 24800 \AA

and the Q(0) H₂ lines. The detector was a 1024×1024 array with a spatial scale of 0.148"/pix and a spectral resolution of 6.5 Å FWHM. In order to assure good sky subtraction, the targets were observed following the classical ABBA technique. Data were reduced using *Eclipse* and *IRAF* routines. First, we corrected for the “electrical ghost” features generated by the detector using the *Eclipse* package. The data were then flat-fielded using a master flat field image following a correction for distortions along and perpendicular to the slit. Wavelength calibration was performed by means of bright OH lines present in the frames. The 1-D spectra were extracted following a similar procedure as that described for the optical data. 1-D spectra were then corrected for telluric absorptions using a telluric standard star observed right before/after the science target. Airmass differences between the standard star and the objects was usually 0.1 or less, except for the case of Circinus, where the airmass difference of the observation centered at 24400 Å was ~ 0.25 . Flux calibration was applied to the data assuming that the observed telluric star continuum was well approximated by a blackbody function of temperature and magnitude equal to that of the telluric star. The derived sensitive function was then applied to the galaxies.

The intrinsic spatial resolution of the optical and NIR spectra was dictated by the seeing at the time of the different integrations. It was determined from the FWHM of the light profile of the standard star observed right before or after the target. This estimate is listed in column 5 of Table 2. The spectral resolution is ~ 100 km s⁻¹ in the optical, ~ 100 km s⁻¹ at 1.96 μm, and ~ 78 km s⁻¹ at 2.48 μm. The RMS of the wavelength calibration is 3 km s⁻¹ for the optical spectra centred at 6230 Å, 1.3 km s⁻¹ for the ones centred at 7950 Å and 4.6 km s⁻¹ for the NIR data. The spatial resolution in the NIR is FWHM $\simeq 0.75''$ and in the optical $\sim 1''$.

3. Results

3.1. Spatial extraction of the coronal line spectra

2-D spectra of each galaxy were averaged in the spatial direction into separate extraction windows. The spatial size of these windows were selected to optimize both signal-to-noise and spatial resolution. The sizes of the extraction window are given in Table 2, column 7, and in general correspond to the achieved spatial resolution (seeing) of the data. In galaxies with strong continuum, to mitigate nuclear scatter light in the off-nuclear spectra, the nuclear extraction window was enlarged by factors between 20% and 100%.

Aperture windows were extracted consecutively north and south the nuclear one. Because of the differences in plate scale between the blue and red detectors in the optical and the near-IR array, besides the effect of seeing variations, the extraction window is different from line to line even within the same object.

Figures 1 to 6 show the extracted spectra along the spatial direction for all the objects in the sample. Usually, one or two extractions ahead of the last one showing extended coronal emission

are plotted. Each spectrum is identified by its distance (in parsecs) to the nucleus, measured from the center of the extraction window to the nuclear peak position. The value following the \pm sign is the radius of the extraction window. The dotted lines mark the position, relative to the systemic velocity of the galaxy, of [Fe VII] 6087 Å and [Fe X] 6374 Å (blue spectra) and [Fe XI] 7889 Å (red spectra). [Fe VII] 5721 Å is also present in all objects. This line is weaker than [Fe VII] 6087 Å and therefore is not shown in any of the figures.

Information about near-infrared coronal lines [Si VI] 19630 Å and [Si VII] 24830 Å is available for three objects in the sample: Circinus, NGC 1068 and NGC 3727. No ESO/ISAAC observations of the remaining galaxies could be scheduled within ESO/Paranal service mode observations. Spectra for those three sources are shown in Figures 7, 8 and 9, respectively. The spatial resolution $\simeq 0.6''$ FWHM is superior than that achieved in the optical; the spectral resolution is comparable, 100 km s^{-1} .

Table 3 lists the size (radius, in parsecs) of the coronal region derived from [Fe VII] 6087 Å, [Fe X] 6374 Å and [Fe XI] 7889 Å, respectively. For comparison, the table also lists the radius of the emitting region measured from [O I] 6300 Å and [S III] 6312 Å. The size derived from the latter is uncertain because the line is intrinsically weak outside the nuclear region. The last column in the table gives the NLR radius based on [O III] 5007 Å line emission data taken from the literature.

Tables 4 and 5 list the FWHM (in km s^{-1} , already corrected for instrumental resolution) of the coronal lines as well as that of [O I] 6300 Å, included for comparative purposes. Also, the shift of the centroid position of each line component relative to the systemic velocity is given. Centroids and FWHMs were estimated after a multi-Gaussian fit to the lines. In most cases, a two Gaussian fit, accounting for a narrow and a broad component, was necessary to improve the reduced χ^2 . In cases of low signal-to-noise, only a single component fit was used. The tables provide the resulting parameters from a two Gaussian fit when that was possible. In [Fe X] 6374 Å the fitting procedure accounts for the presence of [O I] 6363 Å, whose width and flux were fixed according with the values derived for [O I] 6300 Å. Typical errors in the Gaussian centroid position was $\sim 20 \text{ km s}^{-1}$.

3.2. Specifics to each object

3.2.1. *Circinus*

This is the nearest AGN in the sample, allowing us to map the gas emission with a spatial resolution of $\sim 27 \text{ pc}$ in the blue and $\sim 20 \text{ pc}$ in the red. In the optical spectra (Fig. 1), [Fe VII] 6087 Å, [Fe X] 6374 Å and [Fe XI] 7889 Å are prominent and broader than [O I] 6300 Å. All the iron line regions extend several tens of parsec, including [Fe XI], which extends within the central 20 pc radius (Table 3). In contrast, [O I] 6300 Å extends up to 200 pc radius (Figure 1 shows only the central 53 pc region).

The Fe coronal lines are stronger in the north direction, coinciding with the location of the

ionization cone. South of the nucleus, the line spectrum is much weaker due to a combination of extinction by the large dust lanes that cover the southeast region and the presence of a circumnuclear star forming region. This is supported by the weakness of [O I] 6300 Å, which is almost reduced to noise at 100 pc south from the center and the line ratios [N II]/H α and [S II]/H α , almost a factor of two smaller than those at the same distance to the north.

The Si coronal lines [Si VI] and [Si VII] extend to similar distances but the extension is seen equally north and south the nucleus; [Si VII] extends further north, up to 35 pc (Fig. 7). The inferred size of [Si VII] region confirms VLT subarcsec imaging results in this line (Prieto et al. 2005). Indeed, the [Si VII] image reveals a two-side ionization cone, the North-West side being located about 30 pc length within the much larger, one-side only, cone seen in [O III] 5007 Å or H α .

Oliva et al. (1994, 1999) report for Circinus coronal lines widths comparable to those of lower ionization lines, FWHM ~ 100 km s $^{-1}$. As illustrated by Figs. 1 and 7, all the coronal lines show an asymmetric profile with a sharp cut-off at the red side and an extended wing to the blue side - less obvious, e.g., in [O I] 6300 Å. The FWHM of both low and high ionization lines are rather similar, ~ 100 km s $^{-1}$; yet, at one-third of the line maximum, all coronal lines have developed a prominent blue-asymmetric wing, and at 10% of the maximum, this wing extends to ~ 400 km s $^{-1}$ at the nucleus. At this same position to the red, the highest velocity measured is 200 km s $^{-1}$ (the nuclear profile in velocity space is shown in Fig. 11). The same characteristics apply to the Si line profiles. The shape and width of the lines are in excellent agreement with those presented by Mueller Sánchez et al. (2006) on the basis of much higher spatial resolution data obtained from the near-IR integral field spectrograph SINFONI at the VLT. Their nuclear spectrum, which covers a region of ~ 15 pc displays prominent [Si VI] 1.963 μ m, [Al IX] 2.040 μ m and [Ca VIII] 2.32 μ m lines, all showing the same kinematics characteristics, namely, a blue-shifted wing reaching 500 km s $^{-1}$ at the base of the line but only 200 km s $^{-1}$ on the red side (cf. their Figure 8).

As a reference, H $_2$ molecular lines - seen in large number in the ISAAC spectra - are detected up to 150 pc from the centre (only the central 51 pc region is shown in the figures). H $_2$ emission is the strongest at the nucleus, and then fades progressively outwards. At about 20 pc south from the nucleus H $_2$ is slightly enhanced due to the presence of a star forming ring.

3.2.2. NGC 1386

This object is a factor 2 farther than Circinus. The coronal emission was mapped with a spatial scale of $\simeq 70$ pc FWHM (Table 2).

Fig. 2 shows weak extended coronal emission up to 50 pc radius in [Fe X] and [Fe XI], and up ~ 100 pc radius in [Fe VII] (see also Table 3). The extended emission is slightly stronger north of the nucleus than to the south. In contrast, [O I] and [S III] tend to be stronger towards the south. [O III] 5007 Å shows high collimated emission, composed of several blobs distributed in the

north-south direction Schmitt et al. (2003). The brightest [O III] blob is about 1 " north, coinciding with extended [Fe VII] at the same location in the spectra.

The line profiles in the nuclear region are complex: low and high ionization lines show a broad component but [O I] shows in addition a prominent narrow component, $\text{FWHM} \simeq 100 \text{ km s}^{-1}$, whereas [Ar III] and the Fe coronal lines show a broader profile: $300 \text{ km s}^{-1} < \text{FWHM} < \sim 800 \text{ km s}^{-1}$. [Fe VII] 6087 Å, having the highest S/N, shows a double peak profile, with the red peak stronger than the blue one. This double peak is seen up to ~ 80 pc north and south of the nucleus. A double peak profile is also seen in [Fe VII] 5721 Å, which is detected in the spectra but is not shown because it is weaker than [Fe VII] 6087 Å. As reported below, NGC 1068 presents a similar double peak profile in [Fe VII]. The signal-to-noise limits the discussion about the [Fe X] and [Fe XI] profiles, where only a single Gaussian could be fitted to the data. No NIR coronal line observations are available for this object.

3.2.3. NGC 1068

NGC 1068 is at nearly the same distance as NGC 1386 and NGC 3727. The spatial scale achieved in this case is ~ 100 pc in the blue spectra and ~ 80 pc in the red one. A rapid inspection to the optical spectra (Fig. 3) reveals its complexity, dominated by extreme broadening in all, low and high ionization lines. Even at our mid-spectral resolution, it is difficult to characterize the line profiles and their spatial extension due to blending. For example, the FWHM of [Fe VII] is $\simeq 1700 \text{ km s}^{-1}$ whereas that of [O I] is $\sim 1000 \text{ km s}^{-1}$. NGC 1068 shows thus the largest gas velocities in the sample. Hence, most of the coronal emission discussion is limited to [Fe VII] 6087 Å and [Si VII] 2.48 μm since these are the best isolated lines.

[Fe VII] 6087 Å is the most extended CL, up to 210 pc north to the nucleus, but [Si VI] – next in ionization potential – is by far the strongest line, a factor 3 stronger, although covering half that spatial size. All other coronal lines decrease in strength and size of the emitting region with increasing IP, [Fe XI] being the weakest, a factor 30 lower in flux than [Si VI], and the smallest region, less than 40 pc radius (Tables 4 and 5). The characterization of the [Fe X] 6374 Å region is difficult because this line is strongly blended with [O I] 6363 Å. A multiple Gaussian fitting, fixing parameters for [O I] 6363 Å as determined from a fit to the [O I] 6300 Å line, leads to a conservative upper limit of 100 pc radius for the [Fe X] 6374 Å region.

Both [Si VI] 19630 Å and [Si VII] 24830 Å extend north and south of the nucleus up to 100 pc radius (Fig. 8), half the [Fe VII] region but comparable to that of [Fe X] (Table 3). The particular spatial morphology of [Si VII] emission region has been revealed at subarcsec scales by VLT adaptive optics images (Prieto et al. 2005). [Si VI] shows a central three blob structure within the inner 7 pc radius surrounded by diffuse emission up to ~ 70 pc radius. The present spectroscopy just confirms the Si coronal size derived from imaging. The reported size for the [Si VI] 19630 Å region, derived from *NICMOS* imaging (Thompson et al. 2001) is much larger: ~ 300 pc to the south and 200 pc

to the north. However, we believe that Thompson’s et al. image is largely contaminated by the satellite line H_2 19570 Å. This is easily seen in Figure 8, where both lines appear heavily blended. Moreover, Figure 8 shows that at distances larger than ~ 135 pc, only H_2 is detected.

For comparison, [O I] 6300 Å is detected up to 525 pc north and south from the centre (Figure 3 shows a smaller region). All lines are stronger towards the north side of the nucleus, which coincides with the preferential direction of the [O III] line emission and the radio jet.

Undoubtedly the most reliable information about the kinematics of the coronal gas can be derived first from [Fe VII] 6087 Å, which is the best isolated line and second, from [Si VII] 2.48 μm , also isolated but just falling at the edge of the ISAAC detector, hampering the detection of the most redshifted gas.

At the unresolved nucleus, [Fe VII] 6087 Å shows a prominent double-peak profile (FWHM ~ 1700 km s $^{-1}$) on top of a much broader component with FWZI >4000 km s $^{-1}$. The spatially resolved [Fe VII] also shows a double peak component at both north and south of the nucleus (Fig. 3). At first glance, it could be said that the double peak may result from the combination of a large integration window size and a strong velocity gradient. In order to confirm that this peculiar profile structure is real, we have extracted spectra row by row along the spatial direction in the 2-D frame of NGC 1068. At the redshift of this galaxy (see Table 1), each pixel corresponds to a projected distance of about 26 pc. The left panel of Figure 10 shows the resulting spectra mapped up to 250 pc north and 180 pc south of the peak light profile distribution. The fact that the double peak profile in [Fe VII] is detected at scales below the one covered by the integrated spectra of Fig. 3 strongly supports the presence of double peaked coronal lines in NGC 1068. Moreover, it can be seen that the relative distance between the blue and red peaks increases outwards to the north, from ~ 700 km s $^{-1}$ at the nucleus to ~ 1400 km s $^{-1}$ at 180 pc. Note, however, that the shift of the red peak changes little relative to the line centroid. It moves from ~ 500 km s $^{-1}$ in the nucleus to ~ 600 km s $^{-1}$ at 180 pc. In contrast, the blue peak shifts from $\simeq -200$ km s $^{-1}$ to $\simeq -800$ km s $^{-1}$ within the same distance interval. Further to the north, the centroid position of each of the two peaks remains stable, with the red peak being significantly weaker than the blue one. South to the nucleus, the shape of the coronal profile changes significantly if compared to the northern one: the blue peak becomes broader and its centroid position gets closer to the red one. At ~ 100 pc south from the centre, the blue and red peak have a FWHM of ~ 1600 km s $^{-1}$ and ~ 300 km s $^{-1}$, respectively, but the former starts fading gradually. In fact, at 180 pc, only a narrow red peak is visible.

The right panel of Fig. 10 shows equivalent line profiles for [O I] 6300 Å, emphasizing the different kinematics followed by neutral gas. Unfortunately, [O I] 6300 Å is polluted by [S III] 6312 Å, which is separated from the former, in velocity space, by $\simeq 570$ km s $^{-1}$ at rest, which makes uncertain its interpretation. Nevertheless, two main differences arise: first, no evidence of a double peak structure is seen at the nucleus. Second, the centroid position of the line coincides with the systemic velocity of the galaxy and its shift along the spatial direction is consistent with rotation

around the nucleus. The only similarity seen between both profiles is the presence of a narrow read peak that appears at ~ 50 pc to the south and ~ 130 pc to the north. The peak to the north is probably a second narrow [O I] component, judging from a similar component seen in [O I] 6363 Å (see Fig. 3), the component to the south is presumably due to [S III].

For comparison, HST/STIS spectroscopy shows complex [O III] 5007 Å and H β line profiles (Cecil et al. 2002), with multiple broad peak components and persistent line blueshifting, indicating velocities larger than 2000 km s^{-1} at the faintest levels. These complex profiles have their origin in a multitude of knots, many unresolved (size < 4 pc), and filamentary structure seen across the extended narrow line region of the galaxy (cf. HST/FOC [O III] 5007 Å images of NGC 1068). The spatial resolution of the present spectra is poorer, very likely averaging over many of the clouds seen in the FOC image, including mostly those along the jet. However, in velocity space, the [Fe VII] line traces the same complex profile and gas velocities (Fig. 10). Thus, the [O III] and [Fe VII] clouds should be the same.

Summarizing, the high ionization gas, as mapped by [Fe VII], shows clear imprints of an outflowing wind, with the approaching and the receding components visible at different spatial locations, and their speed increasing outward. In contrast, the neutral gas, as mapped by [O I], seems to have a more relax kinematics.

Moving up in IP, the line profiles become narrower (Figs. 3 and 8). Gas velocities traced by [Fe XI] (although the profile is badly affected by telluric absorptions a broad Gaussian fit is feasible) and the silicon lines are in the range $300 \text{ km s}^{-1} < \text{FWHM} < 1000 \text{ km s}^{-1}$. The non-detection of higher velocity components is a limitation of the spatial resolution and signal-to noise: higher velocities components are dumped in the continuum noise. The Si lines follow a similar kinematic as that shown by [Fe VII]: the peak position of the silicon lines are blueshifted to the north and redshifted to the south. However, the profiles do not show the prominent double peak seen in [Fe VII], which is probably because the ISAAC spectra have higher spatial resolution, hence the possibility to spatially separate the blue- and red-shifted components. Still, at certain locations they do show hints for multiple velocity components (e.g. [Si VI] at 45 pc south; [Si VII] at 135 pc north, Fig. 8). Overall, the Si and [Fe VII] line profiles show a broader profile north of the nucleus than south of it (Figure 8); since the radio jet is seen north, the broadening might be associated with the pass of the jet through the gas clouds.

Previously, Marconi et al. (1996) reported FWHM $\sim 1000 \text{ km s}^{-1}$ for both optical and NIR coronal lines, which is lower than those measured in intermediate ionization lines, e.g. [O III] 5007 Å (FWHM $\sim 1500 \text{ km/s}$), in apparent contradiction with the present results. They also reported on systematic line blueshifts that increase with the IP, reaching $\sim 300 \text{ km s}^{-1}$, but such trend is not obvious from the present data.

3.2.4. NGC 3227

This is a Seyfert 1.5 at the same distance as NGC 1068. The spatial resolution achieved was ~ 60 pc in the blue, ~ 40 pc in the red. However, to avoid contamination of scattered light from the broad-line region -traced by $H\alpha$ - in the off-nuclear spectra, a larger extraction window, with diameter of 100 pc in the blue, 80 pc in the red was considered.

NGC 3227 shows the weakest coronal line region in the sample, and it is unresolved at the spatial resolution achieved. Figure 4 exhibits weak [Fe VII] and perhaps [Fe X], the latter being strongly blended with [O I] 6363 Å. [Fe XI] 7889 Å is not detected. The coronal region is restricted to the nuclear window, i.e., within the inner 50 pc radius from the center. [O I] 6300 Å extends along the full length of the slit, i.e., ~ 300 pc radius in both north and south direction (only the inner 130 pc radius is shown in Figure 4).

[Si VI] 19630 Å extends up to 45 pc north of the nucleus, consistent with the [Fe VII] size. [Si VII] 24830 Å is not detected, consistent with the non detection of [Fe XI]. The absence of these high ionization lines indicates that a much softer ionizing continuum illuminates the NLR, lacking photons with energies ≥ 200 eV, than in the other galaxies of the sample.

For assessing the kinematics, [Fe VII] is the best isolated and higher S/N line. It is nevertheless affected by telluric residuals on its red side. A Gaussian fit to the line indicates a FWHM $\simeq 900$ km s^{-1} , almost a factor 2 larger than that of [O I] 6300 Å (Table 4), and a centroid blueshifting of -125 km s^{-1} .

3.2.5. NGC 3783 and MCG-6-30-15

These two galaxies are the more distant and the only Type 1 Seyfert of the sample. The spatial resolution achieved was about 100 pc for MCG6-30-15, ~ 200 pc for NGC 3783. The actual spatial bin used in these cases is 20-50% larger than the spatial resolution (Table 2), in order to prevent off-nuclear spectra get contaminated by nuclear light. The nuclear windows are set by summing up all the spectra containing broad $H\alpha$ emission. No NIR spectra are available for these objects.

NGC 3783 (Figure 5) presents the largest coronal line region, with more than 400 pc radius in the [Fe VII] 6087 Å line - this is also confirmed by [Fe VII] 5721 Å line, present in all our spectra but not shown for sake of simplicity. [Fe X] and [Fe XI] are also extended but to about half radius (Table 3). [O III] 5007 Å, however, is distributed in a halo around the nucleus, extending up to a radius of 140 – 175 pc (HST image in Schmitt et al. (2003)). This is about a factor 2 smaller than the [Fe VII] region. We suspect that an over subtraction of the continuum image is removing [O III] emission from the outer regions of the halo. We note that e.g., [Ar III], (Figure 5), is already very prominent at 210 pc from the nucleus.

The iron coronal lines are broader than [O I] by about a factor of 2. At the nucleus, they

show a broad-blueshifted wing with FWHM $\sim 1000 \text{ km s}^{-1}$. At all spatial locations, the coronal peak position is systematically shifted to the blue by more than 100 km s^{-1} (Table 4). [O I] 6300 Å shows a clear double-peak profile, but [Fe VII] does not: coronal gas is clearly more turbulent than neutral gas, a double peak in [Fe VII] may be masked by the large width of the line.

In *MCG-6-30-15* (Fig. 6), the Fe coronal line emission is unresolved and thus restricted to the inner 100 pc radius in [Fe VII] and [Fe X] and less than 50 pc radius in [Fe XI]. In contrast, [O I] 6300 Å and [S III] 6312 Å extend up to 300 pc north and south from the centre (this emission is not easily seen in Fig. 6 but cuts were chosen not to overcrowd the figure). These low-ionization lines are also narrow, FWHM $\sim 100 \text{ km s}^{-1}$, and symmetric whereas the Fe coronal lines show the typical blue wing, with FWHM $\sim 1500 \text{ km s}^{-1}$ (Table 4). Both, the narrow and the broader component of the Fe lines, show a systematic blueshifting; that of the narrow component increases with IP, up to -140 km s^{-1} in [Fe XI]; the shift of the broad component is more uniform with IP, but larger, in the range of $\sim -300 \text{ km s}^{-1}$.

4. The size of the coronal line region

Table 3 provides a compilation of the sizes of the coronal line regions derived in this work. The table includes also coronal sizes derived from the high spatial resolution [Si VII] 2.48 μm imaging of Prieto et al. (2005). The smallest “resolved” coronal region is found in Circinus, with a radius of ~ 20 pc; the largest is found in NGC 3783, with radius of 400 pc. Overall, the coronal region size average in the 100 pc range. At each individual object, the CLR size decreases with increasing ionization potential, i.e., the hardest the photons the closer to the nucleus the highly ionized ions are created.

Lower ionization lines extend to much larger radius in Seyfert galaxies, from several hundred pc to kpc. Table 3 also includes the sizes of [O I] 6300 Å and [S III] 6312 Å line regions extracted from the present data, and that of [O III] 5007 Å taken from the literature. The coronal line region is at least a factor 2–3 smaller than that of [O III] or [O I]. The most extreme case is Circinus, with a coronal region a factor 10 smaller than that of [O III].

These differences in sizes indicate a very stratified NLR, namely, lines with IP larger than 100 eV are restricted to the inner 100 pc radius whereas medium ionization gas, i.e, IP < 54 eV, extends to a region at least twice that value. Lines with IP < 30 eV, extend over a region comparable or larger than that of the medium ionization lines. Photoionization produces this type of stratification, and thus it should be the principal source of gas excitation in these galaxies.

Besides stratification, the ionized gas in Seyfert galaxies is known to be collimated in large nuclear bicones seen in H α or [O III]. We know from previous work based on long-slit spectroscopy carried out in directions both along and perpendicular to the ionization cone (Reunanen et al. 2003), and from direct imaging in the [Si VII] 2.48 μm line (Prieto et al. 2005), that the coronal emission tends to extend preferentially along or within the ionization cone traced by medium-ionization gas.

Indeed, the latter work shows that the coronal gas is more collimated than the medium ionization gas.

5. Kinematics of the coronal gas

Coronal lines are, in general, identified with a broad and blueshifted profile. Assuming that the emission comes from an unresolved nuclear region, the systematic blueshifting has been interpreted as an outflowing wind provided that nuclear obscuring material prevent us for seen the receding flow (e.g., Penston et al. 1984; Evans 1988; Erkens et al. 1997; Rodríguez-Ardila et al. 2002).

The present spectroscopic data conforms with this prototype coronal profile albeit with some added complexity. This can be seen in Figure 11 , where the “nuclear” profiles of the best defined coronal lines for the objects in the sample are compared. For reference purposes, the profile of a lower-ionization line is also included in the Figure. In all objects a velocity-shift was applied to the centroid positions to bring them all to $V=0 \text{ km s}^{-1}$. Figure 11 shows that all coronal lines are asymmetric and broader than the reference, low-ionization line. In most cases, the profiles display a prominent blue asymmetry. At 20% of peak intensity, the blue wing extends up to 1200 km s^{-1} while the red one goes only up to 600 km s^{-1} . The less extreme case is Circinus: at 20% of maximum, the blue and red wings extend only to 250 km s^{-1} and 100 km s^{-1} , respectively. The most extreme one is NGC 1068, with blue and red wings extending in velocities up to 2000 km s^{-1} ; the FWZI is larger than 4000 km s^{-1} . NGC 1068 and NGC 1386 are the only two objects displaying a double peak coronal profile, easily seen in [Fe VII] at both the nuclear and extended regions. To our knowledge, no previous detection of this such type of coronal line profile has been reported for any other Seyfert.

The points below summarize the main kinematic results:

1. In cases of high signal-to-noise and not blending, coronal line profiles could be fit with a two Gaussian component: a narrow one with FWHM comparable to, or slightly larger than, that of the lower ionization lines, and a broad, usually blueshifted, component with FWHM ranging from 700 km s^{-1} (e.g Circinus) to 1500 km s^{-1} (e.g MCG-6-30-15 or NGC 3783) and centroid shifts in the range $100\text{--}600 \text{ km s}^{-1}$. The centroid position of the narrow component remains in general at the systemic velocity, as it is the case for the neutral gas lines, [O I] in the optical, H_2 in the near-infrared.

2. Blueshifting of the coronal emission is also seen in the spatial resolved emission, and at both sides of the nuclear region along the slit position (e.g., Circinus, NGC 1068 and NGC 3783). If the emission is a rather collimated wind, blueshifting at both sides of the nucleus would require the axis of the wind to be rather close to the plane of the sky in Type 2 objects, or close to the line of sight in Type 1. As the counterpart receding gas is usually not seen, this requires the presence of obscuring material at the base of the wind.

3. One would expect an increase of the coronal line width with ionization potential, as the higher the ionization potential the closer to the ionization source the line is formed. Gas velocities should then approach those of the broad line region. No such trend is generally seen in the data. As Fig. 11 illustrates, the Seyfert 1s MCG-6-30-15 and NGC 3783 show an increase in line width with ionization potential whereas in the Type 2 sources of the sample, the opposite is found. However this could be an obscuration effect in Type 2 objects, which will affect mostly the higher ionization lines because they are formed closer to the center.

4. The kinematics of NGC 1068 deserves special attention. The best coronal emission kinematics is traced by [Fe VII]. The line profile both north and south of the nucleus shows a double peak component, visible up to ~ 250 pc and ~ 180 pc, respectively, each tracing blueshifted and redshifted gas. This type of profile has not ever been reported in the literature for a Seyfert galaxy. One could think of several geometries to account for this complex kinematics, e.g., gas moving in circular orbits in a thick toroid with the rotation axis close to the north-south direction, leading to a double peak spectrum at both sides of the nucleus. Alternatively, radial motions within a cone with its axis closely oriented to the plane of the sky could lead to a double peak spectrum at different spatial locations corresponding to approaching and receding gas. Observational evidence found from polarimetry and the correlation between the NLR emission maps and the radio structure supports the later scenario.

5. For the three galaxies for which optical and NIR spectra are available: Circinus, NGC 1068, and NGC 3727, the comparison of the respective coronal spectra indicates little extinction in the coronal region. This is based on the following arguments. First, coronal lines of comparable ionization potential are equally present in the optical as in the NIR, e.g. [Fe VII] and [Si VI]. Second, the coronal region extends to similar sizes in the optical as in near-IR. Third, in Circinus, optical and NIR coronal lines present comparable line profile. Considering that the extinction is reduced by about 6 magnitudes between these two spectral regions, differences in the dispersion velocities due to differences in optical depth should be expected. It follows that optical coronal lines should be narrower than their NIR counterparts, which is not the case.

6. Is photoionization driving the coronal line emission?

Coronal lines are collisionally excited and can be produced either by a gaseous region photoionized by a hard UV continuum (Ferguson et al. 1997), a hot ionized plasma (Viegas-Aldrovandi & Contini 1989) or a mix of both (Contini et al. 1998a). Radiation from the central source alone cannot explain, however, the systematic blueshifting of the lines. An alternative approach still invoking photoionization was suggested by Binette (1998), who proposed that radiation pressure from the central engine generates a strong density gradient within the photoionized structure and is responsible for accelerating the matter-bounded gas (the zone of high excitation), explaining the systematic blueshift observed for coronal lines.

Moreover, constraints set by the observations regarding the nature of the coronal regions are: the size of the emitting clouds are expected to be less than 2 pc in Circinus and less than 7 pc in NGC 1068 – on the basis of the spatial resolution achieved in the [Si VII] images by Prieto et al. (2005). Cloud velocities, if reflecting any NLR velocity field of accelerating gas, should reach up to 1000 km s⁻¹.

In order to investigate the most plausible scenario for the production of the coronal lines taking into account the above constrains, we first tested the possibility that the coronal region, which extends up to several tens of parsecs from the central engine, can be produced by pure photoionization. To this purpose, models with the AANGABA code (Gruenwald & Viegas 1992) were run. The ionizing spectrum suggested by Oliva et al. for Circinus (1999, see their Fig. 7) was adopted; solar values (Grevesse & Anders 1989) were assumed for the gas chemical abundances.

Two values for the luminosity of the ionizing radiation were adopted: $L_{\text{ion}} = 10^{43.5}$ erg s⁻¹ and $10^{44.5}$ erg s⁻¹, as used e.g. by Ferguson et al. (1997) and Oliva et al. (1999) in their respective photoionization models. The number of ionizing photons, Q_{H} , contained by those two spectral energy distributions are 2.5×10^{53} and 2.5×10^{54} phot s⁻¹, respectively. A grid of models was built with the density in the range 10^2 cm⁻³ to 10^6 cm⁻³, and the ionization parameter $U = \Phi_{\text{H}}/nc$ from 10^{-3} to 1, where Φ_{H} is the flux of ionizing photons reaching the coronal region, defined as $\Phi_{\text{H}} = Q_{\text{H}}/4\pi D^2$, D being the distance from of the emitting cloud to the central source, assuming the covering factor unity. For each Φ_{H} - or equivalently L_{ion} - there is a relation between U , n and D (see, for example, Ferguson et al. 1997). This means that for a given AGN, i.e., a given L_{ion} , U is not a free parameter anymore if we know D from the spatially resolved observations. The U , n and D relation is given in Figure 12. Since coronal lines require high ionization parameters (Ferguson et al. 1997), the distance from the nucleus to the CL emitting cloud is limited, as we shall see below.

With the above parameters in mind, the distribution of the fraction of iron and silicon ions producing the observed coronal lines versus the size of the emitting cloud was computed. The results are shown in Figure 13 and 14, respectively, for $n_{\text{e}} = 10^4$ cm⁻³ and $U = 10^{-2}$, 10^{-1} and 1. Ion fractions for models with $U = 10^{-2}$ (panel c) and the two values of L_{ion} coincide, and Fe⁺¹⁰ is not present in these clouds. A density of $n_{\text{e}} = 10^4$ cm⁻³ is taken as face value following the estimate derived for Circinus from [Ne V] $14.3\mu\text{m}/24.3\mu\text{m}$ (Moorwood et al. 1996). Moving to higher densities will press more for higher ionization parameters, but in that case, following Figure 12, it will be difficult to explain the spatial extension of the coronal region.

It can be seen from Figs 12 and 13 that only the single-cloud models with $U \geq 0.1$ show Fe⁺⁶, Fe⁺⁹ and Fe⁺¹⁰. Clouds with lower values of U tend to be dominated by Fe⁺⁶ and less ionized species. The distributions of Si⁺⁵ and Si⁺⁶ are similar to that of Fe⁺⁶. The Figures also show that the geometrical width of the clouds emitting the coronal lines is less than 1 pc for $U = 0.1$ and less than 5 pc for $U = 1$, if $n_{\text{e}} = 10^4$ cm⁻³.

Notice that the lower the density, the wider the coronal region size. Considering $U \leq 0.1$ and an average coronal region size of 150 pc, it appears that a density of $n_{\text{e}} = 10^4$ cm⁻³ is too large to

account for the observed dimensions (Fig. 12). We thus conclude that densities down to at least $n_e = 10^3 \text{ cm}^{-3}$ are required. Lower densities will lead to even larger regions, but that will penalize line detection - as the emission is proportional to n_e^2 . Larger distances could be reached if the filling factor were low. Yet, very high spatial resolution images in [Si VII] $2.48 \mu\text{m}$ of Seyfert galaxies (Prieto et al. 2005) show that the coronal emission is not yet resolved in blobs/ knots at spatial scales of 10–15 pc, but shows instead diffuse morphology. With such low surface brightness it will be difficult to detect any emission if the filling factor were low.

Thus, assuming that lines from different ionization potential ions, e.g., [Fe VII], [Fe X] and [Fe XI], *are all produced in the same cloud*, a cloud density of $n_e = 10^3 \text{ cm}^{-3}$, and U between 0.1 and 1, according to Figure 12 the maximum size of the coronal line region is $\leq 100 \text{ pc}$ for the brighter source ($L_{\text{ion}} = 10^{44.5} \text{ erg s}^{-1}$), and $\leq 30 \text{ pc}$ for the dimmer one if it is powered entirely by photoionization.

Diagnostic diagrams based on flux ratios between the three optical iron lines provide a good test to the photoionization models and are shown in Fig. 15. Because of the relationship between U , n and D , the loci of the results from all the models are represented by the same curve (dashed). On this curve, the dots correspond to different values of U ($\log U = -2, -1.5, -1, \text{ and } 0$) for $n_e = 3 \times 10^3 \text{ cm}^{-3}$ and $L_{\text{ion}} = 10^{44.3} \text{ erg s}^{-1}$. Note that a density of $3 \times 10^3 \text{ cm}^{-3}$ was chosen because it is located between the two limiting cases, i.e., 10^3 and 10^4 cm^{-3} . Data plotted in this Figure are extracted from Table 4. The line ratios show an ample disagreement with these standard photoionization models.

The only way to single-cloud photoionization models reproduce the iron line ratios is to find a way to shift the photoionization results up and left on both panels of Fig. 15. This could be achieved with an increase of the [Fe XI] line with respect to the [Fe VII] line, and the later relative to [Fe X]; or the opposite: a decrease of the [Fe X] line with respect to [Fe VII] and [Fe XI]. Our results were obtained using effective collision strengths calculated using the distorted wave method (Krueger & Czyzak 1970; Nussbaumer & Storey 1982). More recently, atomic data for those lines have been available in the literature, mainly due to the so called Iron Project (Hummer et al. 1993). These calculations are carried out using the R-matrix method and account for resonances. These resonances tend to increase the excitation cross-sections, and the net effect is an increase of the collision strengths, mainly at lower temperatures (Arggawal et al. 2003; Berrington et al. 2000; Pelan et al. 2001). A close look into the new data shows that indeed the new collision strengths are higher than the values used in this paper, as expected. Compared to the previous values used in our calculations, the increase is more significant for Fe X than for the lines of the other two ions, Fe XI being the second one more affected. Thus, the [Fe X]/[Fe VII] ratio should increase if calculated with new atomic data, as well as [Fe XI]/[Fe VII], although by a smaller factor. On the other hand, [Fe XI]/[Fe X] should decrease. In brief, the overall tendency is to shift the photoionization results presented in Fig. 15 (dashed line) to the right, leading to a larger disagreement with the observational data.

We then consider the additional effect of shock excitation “coupled” with photoionization to explain the coronal emission. As a constraint, we assumed that the observed velocity width (at FWHM) measures the actual shock velocity that passes through the gas, which should then be in the range 300 to 900 km s⁻¹. The resulting composite models are also shown in Fig. 15 (solid line). They were generated using the code SUMA, which accounts for the coupled effect of shock and photoionization (Viegas & Contini 1997). In these composite models L_{ion} has the same values as those used in the pure photoionization models.

If the coronal region clouds are shock dominated, there is no upper limit for the distance of the coronal emission to the nucleus as there is for the pure photoionization case. In order to limit the average cloud density to 10⁴ cm⁻³, models with shock velocities higher than 500 km s⁻¹ were built assuming a preshock density $n_0 = 200$ cm⁻³, while for lower velocities, $n_0 = 300$ cm⁻³ was assumed. Models shown in Figure 15 illustrate the contributive effect of shocks to excite coronal lines in the shock-dominated case. A composite effect of shock and photoionization potentially offers then a better agreement of the observed iron line flux ratios. Notice that the effect of the newer collision strength data is less important in the post-shock region, where the iron coronal lines are produced, because the temperature is higher than in the photoionized zone. A smaller shift of the shock-dominated curve to the right would indicate that velocities lower than 300 km s⁻¹ should probably also be included.

The models presented provided a first insight into the physical processes powering the CLR. Self-consistent models for a given object would require a more comprehensive analysis of the whole emission-line spectrum, which is out of the main focus in this paper. As already discussed for some AGN (Contini et al. 1998a,b, 2003), we expect that photoionization as well as shock must contribute to the physical conditions of the different types of emitting clouds present in the NLR. The results shown in Figure 15 support this scenario.

7. Concluding remarks

- Coronal lines are expected to be presented in all type of AGN. This work surveyed at unprecedented spectral and spatial resolution, five coronal lines covering a large range both in ionization potential, between 100 and 260 eV, and wavelength (optical and NIR regions) in six Seyfert galaxies: three Type 2, two Type 1 and one Type 1.5. We found that they are all present in the galaxies with the exception of NGC 3727, where only ions from the lowest ionization potentials are detected. Thus, the shape, or hardness, of the ionizing spectrum in Seyfert galaxies is very similar regardless of the type. This is in the same line as found by (Prieto & Viegas 2000) in a different sample of Seyfert galaxies, after the analysis of IR-ISO coronal lines spanning a range in ionization potential between 54 and 300 eV. NGC 3727 is the only case showing very soft ionizing spectrum as only lines from the lowest IP are present.
- The coronal region is spatially resolved over scales that range from a few tens of parsecs up

to a few hundreds of parsecs from the center. The size of the emitting region varies with the ionization potential: the highest the ionization potential the most compact the region becomes. This stratification indicates that nuclear photoionization is the principal excitation mechanism.

- Coronal line profiles are characterized by two components: a narrow one whose centroid and FWHM values are within the range found for lower ionization lines, and a broader one, whose centroid is systematically shifted to the blue by a few hundreds of km s^{-1} and has a FWHM a factor 2 at least larger than that of the lower ionization lines. The gas velocities implied by this component vary from object to object, and are in the range from 500 up to 2000 km s^{-1} . This blueshifting is interpreted as an outflowing wind. However, a nuclear wind should have an approaching and a receding component. As the blueshifted component is the one often seen, the redshifted one has to be obscured by dust at the base of the wind.
- We are however able to see the receding component of the wind in two objects: NGC 1068 and NGC 1386. This interpretation comes from the detection of a spatially resolved double peak in the [Fe VII] line, each peak tracing respectively blueshifted and redshifted gas at each spatial location. A spatially resolved double peak could be produced by gas moving in circular orbits in a thick toroid with the rotation axis close to the north-south direction, or by radial motions along a collimated cone, with the axis closely oriented to the plane of the sky. The observational evidence supports this latter scenario.
- For a luminosity of the ionizing radiation source in the range $10^{43.5} - 10^{44.5} \text{ erg s}^{-1}$, single-cloud photoionization models indicate that to produce detectable coronal emission over a wide range of ionization potentials, the ionization parameter must be larger than 0.1 and the density should be larger than 10^3 cm^{-3} . Under these conditions, such simple single-cloud models can account for coronal emission of up to 100 pc from the nucleus if the ionizing radiation luminosity is higher than $10^{44} \text{ erg s}^{-1}$. For lower luminosities the size of the coronal regions can at most reach 50 pc, which is smaller than the results obtained for some of the galaxies of our sample. In addition, these models fail to explain the observed Fe line ratios. Furthermore, even multi-cloud photoionization models, mimicking the stratification of the NLR, can hardly reproduce the observations, leading us to conclude that another energy source must be present.
- In support to the above result, diagnostic diagrams using the Fe lines show that single-cloud photoionization models largely depart from the trend shown by the data. However, if the contribution of additional shock excitation is included, with shock velocities between 300 and 900 km s^{-1} in agreement with observations, the *combined* photoionization plus shock effect is able to account for the observed ratios.
- It is interesting to remark that the systematic presence of H_2 lines in the nuclear region of AGN implies very large variations in the physical conditions of the gas, capable of sustaining highly ionized species along with molecules which easily dissociate with the radiation of the

central engine. The molecular H₂ emission clearly relates to a different type of clouds from that traced by the ionized gas, on the basis of both its kinematic - low rotation, narrow line widths - and spatial distribution which usually extends over several hundreds parsecs to kpc from the nucleus, and preferentially in directions perpendicular to the ionization cone (Reunanen et al. 2002, 2003; Rodríguez-Ardila et al. 2004, 2005).

This research has been partly supported by the Brazilian agencies FAPESP (00/06695-0) to SV and RW, CNPq (304077/77-1) to SV and CNPq (309054/03-6) to ARA. This research has made use of the NASA/IPAC Extragalactic Database (NED) which is operated by the Jet Propulsion Laboratory, California Institute of Technology, under contract with the National Aeronautics and Space Administration.

REFERENCES

- Aggarwal, K. M., & Keenan, F. P., 2003, MNRAS, 338, 313
- Berrington, K. A., Nakazaki, S., & Norrington, P. H. , 2000, A&AS, 142, 313
- Binette, L. 1998, MNRAS, 294, L47
- Cecil, G., et al., 2002, ApJ, 568, 627
- Contini, M., Prieto, M. A., & Viegas, S. M. 1998a, ApJ, 505, 621
- Contini, M, Prieto, M.A., & Viegas S.M. 1998b, ApJ, 492, 511
- Contini, M., Rodríguez-Ardila, A., & Viegas, S. M. 2003, A&A, 408, 101
- De Robertis, M. M., & Osterbrock, D. E. 1986, ApJ, 301, 727
- Erkens, U., Appenzeller, I., & Wagner, S. 1997, A&A, 323, 707
- Evans, I.N. 1988, ApJS, 67, 373
- Ferguson, J. W., Korista, K. T., & Ferland, G. J. 1997, ApJS, 110, 287.
- Freeman, K.C., Karlsson, B., Linga, G., Burrell, J. F., van Woerden, H. & Goss W. M. 1977, A&A, 55, 445
- Grevesse, N. & Anders, E. 1989, *Proc. of the AIP Conference on Cosmic Abundances of Matter*, 183, American Institute of Physics: New York, 1
- Gruenwald, R. & Viegas, S. M. 1992, ApJS, 78, 153

- Hummer, D. G., Berrington, K.A., Eissner, W., Pradhan, A. K., Saraph, H. E., et al. 1993, A&A, 279, 298
- Kishimoto M., 1999, ApJ, 518, 676
- Kreuger, T. K., Czyzak, S. J. Proc. R. Soc. London Ser. A318, 531
- Marconi, A., van der Werf, P. P., Moorwood, A. F. M., & Oliva, E. 1996, A&A, 315, 335
- Moorwood, A. F. M., et al., 1996 A&A, 315, L109
- Mueller Sánchez, F., et al., 2006, A&A, *in press*, (astro-ph/0604317)
- Mundell, C. G., Holloway, A. J., Pedlar, A., Meaburn, J., Kukula, M. J., et al. 1995, MNRAS, 275, 67
- Nussbaumer, H., & Storey, P. J., 1982, A&A113, 21
- Oliva, E., Marconi, A., & Moorwood, A. F. M. 1999, A&A, 342, 87
- Oliva, E., Salvati, M., Moorwood, A. F. M., & Marconi, A. 1994 A&A, 288, 457
- Pelan, J. C., & Berrington, K. A., 2001, A&A365, 258
- Penston, M., Fosbury, R. A. E., Boksenberg, A., Ward, M. J., & Wilson, A. S. 1984 MNRAS, 208, 347
- Peterson, B. et al. 2004, ApJ, 613, 682
- Porquet, D., Dumont, A.-M., Collin, S., Mouchet, M. 1999, A&A, 341, 58
- Prieto, M.A., Marco, O. & Gallimore, J. 2005, MNRAS, 364, L28.
- Prieto, M.A. & Viegas, S. 2000, ApJ, 532, 238
- Reunanen, J., Kotilainen, J. K., Prieto, M. A. 2002, MNRAS, 331, 154
- Reunanen, J., Kotilainen, J. K., Prieto, M. A. 2003, MNRAS, 343, 198
- Rodríguez-Ardila, A., Viegas, S. M.; Pastoriza, M. G., Prato, L. 2002, ApJ, 579, 214
- Rodríguez-Ardila, A., Pastoriza, M. G., Viegas, S., Sigut, T. A. A., Pradhan, A. K. 2004, A&A, 2004, 425, 457
- Rodríguez-Ardila, A., Riffel, R., Pastoriza, M. G., MNRAS, 2005, 364, 1041
- Schmitt, H. R., Donley, J.L., Antonucci, R., Hutchings, J. B., Kinney, A. 2003, ApJS, 148, 327
- Thompson, R., Chary, R.-R., Corbin, M. R., & Epps, H. 2001 ApJ, 558, 97

Veilleux S., Bland-Hawthorn, J. 1997, ApJ, 479, 105

Viegas-Aldrovandi, S., & Contini, M. 1989 ApJ, 339, 689

Viegas, S., & Contini, M. 1997, ASPC, 113, 365

Table 1. Properties of the Seyfert galaxies studied in this work.

| Name | Seyfert Type | pc/'' | z | PA (°) ^a |
|-------------|--------------|-------|----------------------|---------------------|
| CIRCINUS | 2 | 19 | D~4 Mpc ^b | -44°NW |
| NGC 1386 | 2 | 56 | 0.00289 | 0°N-S |
| NGC 1068 | 2 | 75 | 0.00379 | 35°NE |
| NGC 3227 | 1.5 | 74 | 0.0038 | 10°NE |
| MCG-6-30-15 | 1 | 105 | 0.00775 | -65°NW |
| NGC 3783 | 1 | 192 | 0.00973 | -10°NW |

^aDerived from [O III] 5007 Å line images.

^bFreeman et al. (1977)

Table 2. Log of Observations.

| Galaxy | Date of Obs. (dd/mm/year) | Telescope | Instrument | Seeing ('') | Airmass | D ¹ ('') | λ _c (Å) | exp. time sec. |
|-------------|------------------------------|-----------|------------|----------------|---------|------------------------|-----------------------|-------------------|
| (1) | (2) | (3) | (4) | (5) | (6) | (7) | (8) | (9) |
| NGC 1068 | 31/01/2002 | ESO-NTT | EMMI | 1.33 | 1.40 | 1.4 | 6230 | 4×400 |
| | 10/03/2002 | ESO-NTT | EMMI | 0.98 | 1.10 | 1.1 | 7890 | 4×400 |
| | 24/11/2001 | ESO-VLT | ISAAC | 0.72 | 1.21 | 0.6 | 19800 | 10×60 |
| | 24/11/2001 | ESO-VLT | ISAAC | 0.60 | 1.15 | 0.6 | 24400 | 10×60 |
| CIRCINUS | 28/02/2002 | ESO-NTT | EMMI | 1.25 | 1.24 | 1.4 | 6230 | 4×400 |
| | 28/02/2002 | ESO-NTT | EMMI | 0.91 | 1.25 | 1.1 | 7890 | 4×400 |
| | 06/04/2002 | ESO-VLT | ISAAC | 0.63 | 1.33 | 0.9 | 24400 | 10×60 |
| | 06/04/2002 | ESO-VLT | ISAAC | 0.63 | 1.32 | 0.9 | 19800 | 10×60 |
| NGC 1386 | 27/11/2001 | ESO-NTT | EMMI | 1.20 | 1.01 | 1.4 | 6230 | 4×400 |
| | 27/11/2001 | ESO-NTT | EMMI | 0.98 | 1.00 | 1.1 | 7890 | 4×400 |
| NGC 3227 | 28/02/2002 | ESO-NTT | EMMI | 0.92 | 1.55 | 2.1 ^a | 6230 | 4×400 |
| | 28/02/2002 | ESO-NTT | EMMI | 0.93 | 1.53 | 1.6 ^a | 7890 | 4×400 |
| | 10/02/2002 | ESO-VLT | ISAAC | 0.56 | 1.48 | 0.6 | 19800 | 10×120 |
| | 10/02/2002 | ESO-VLT | ISAAC | 0.56 | 1.48 | 0.6 | 24400 | 10×120 |
| NGC 3783 | 10/03/2002 | ESO-NTT | EMMI | 1.13 | 1.06 | 1.4 | 6230 | 4×400 |
| | 10/03/2002 | ESO-NTT | EMMI | 0.95 | 1.15 | 1.1 | 7890 | 4×400 |
| MCG-6-30-15 | 28/02/2002 | ESO-NTT | EMMI | 1.05 | 1.08 | 2.1 ^a | 6230 | 4×400 |
| | 28/02/2002 | ESO-NTT | EMMI | 1.00 | 1.02 | 1.6 ^a | 7890 | 4×400 |

¹D is the diameter of the extraction window used to define the nuclear spectrum and those of adjacent regions. Spectra shown in Fig. 1 to 9 are extracted according to this value.

^aAperture size for the nuclear spectrum. Spectra for the extended regions were extracted using a window size of 1.4'' and 1.1'' for the blue and red regions respectively

Table 3. Size (radius in pc measured from the nucleus) of the coronal and lower ionization line regions in Seyfert galaxies¹. References are provided for those values taken from the literature.

| Object IP(eV) | [Fe VII] 100 | [Fe X] 240 | [Fe XI] 260 | [Si VI] 170 | [Si VII] 205 | [O I] 0.0 | [S III] 24 | [O III] 35.1 |
|------------------|-----------------|---------------|----------------|----------------|----------------------------|--------------|-----------------|-------------------|
| Circinus | 53 N-27 S | 27 N-S | 21 N-S | 17 N-S | 35 N-17 S | 200 | 27 ² | >500 ^a |
| NGC 1386 | 108 N-49 S | 49 N-S | 53 N-38 S | NA | NA | 235 | 157 | 165 ^b |
| NGC 1068 | 210 N-105 S | <~100 | <~40 | 90 N-135 S | 135 N-S | 525 | 210 | 375 ^b |
| NGC 3227 | <78 | <78 | ... | 45 N | ... | 300 | 106 | 518 ^c |
| NGC 3783 | 437 N-302 S | 235 N-302 S | 120 N | NA | NA | 540 N-270 S | <135 | 175 ^b |
| MCG-6-30-15 | <~90 | <~90 | <50 | NA | NA | ~300 | ~300 | 295 ^b |
| NGC 3081 | | | | | 120 N ^d | | | |
| ESO428-G014 | | | | | 120 NW-160 SE ^d | | | |

¹N-S mean same distance to the North and South, NA = not available. [O III] 5007 Å sizes are measured from imaging data. [Si VII] images exist only for the four objects quoted in the table, two of them are not included in this spectroscopy study, the other two, Circinus and NGC 1068 show comparable size to that reported here from spectroscopy.

²This value is one order of magnitude smaller than the one determined by Oliva et al. (1999) using [S III] 9531 Å. The large discrepancy between the two sizes is likely due to the slit orientation, which in our case is along the edge of the ionization cone (PA=-7deg) while in Oliva et al. (1999) is along its axis (PA=-44deg). Clearly, the [S III] 9531 Å emission is highly anisotropic and it seems to follow that of [O III] 5007 Å (see Figure 1 of Oliva et al. (1999)).

^aVeilleux & Bland-Hawthorn (1997)

^bSchmitt et al. (2003)

^cMundell et al. (1995)

^dPrieto et al. (2005)

Table 4. FWHM and shifts ^a from the centroid position (both in km/s), and fluxes (in units of 10^{-15} erg cm⁻² s⁻¹) for the optical coronal and [O I] 6300 Å lines measured in the nuclear and adjacent regions in the galaxy sample.

| Aperture (1) | [Fe VII] | | | [O I] | | | [Fe X] | | | [Fe XI] | | |
|-----------------|-------------|-------------------|-------------|-------------|-------------------|-------------|-------------|-------------------|--------------|--------------|--------------------|--------------|
| | FWHM (2) | ΔV (3) | Flux (4) | FWHM (5) | ΔV (6) | Flux (7) | FWHM (8) | ΔV (9) | Flux (10) | FWHM (11) | ΔV (12) | Flux (13) |
| Circinus | | | | | | | | | | | | |
| NUC | 120 | -15 | 1.14±0.10 | 105 | 0.0 | 6.23±0.10 | 140 | 32 | 2.30±0.12 | 105 | -11 | 3.82±0.14 |
| | 400 | -250 | 1.11±0.45 | ... | ... | ... | ... | ... | ... | 290 | -130 | 1.83±0.36 |
| 27 pc N | 290 | -84 | 0.77±0.15 | 110 | -38 | 1.86±0.11 | 135 | 20 | 0.55±0.12 | 160 | -70 | 0.50±0.14 |
| 53 pc N | 130 | -79 | 0.20±0.06 | 135 | -76 | 0.85±0.12 | ... | ... | ... | ... | ... | ... |
| 27 pc S | 160 | 20 | 0.49±0.10 | 105 | 24 | 2.37±0.10 | 120 | 60 | 1.07±0.10 | 105 | 0.0 | 1.36±0.11 |
| | ... | ... | ... | ... | ... | ... | ... | ... | ... | 180 | -150 | 0.50±0.08 |
| NGC 1386 | | | | | | | | | | | | |
| NUC | 740 | 81 | 6.88±1.08 | 105 | -35 | 1.20±0.19 | 580 | -100 | 2.41±0.80 | 250 | -120 | 1.57±0.50 |
| 78 pc N | 220 | 290 | 0.70±0.21 | 575 | 87 | 1.87±0.50 | ... | ... | ... | 320 | -45 | 0.69±0.11 |
| | 1410 | -180 | 3.08±1.20 | ... | ... | ... | ... | ... | ... | ... | ... | ... |
| 78 pc S | 700 | 173 | 1.03±0.08 | 105 | -43 | 3.40±0.16 | ... | ... | ... | 280 | -105 | 0.59±0.34 |
| NGC 1068 | | | | | | | | | | | | |
| NUC | 1670 | -39 | 142.0±17.3 | 900 | 0.0 | 173.9±9. | 1595 | -150 | 47.8±17.0 | 760 | -165 | 16.4±1.3 |
| 105 pc N | 1450 | -250 | 81.0±11.5 | 1020 | -50 | 177.1±8.4 | 1380 | -175 | 28.5±11.3 | 680 | -165 | 4.1±1.4 |
| 210 pc N | 990 | -695 | 14.3±2.3 | 1280 | -30 | 44.2±3.2 | ... | ... | ... | ... | ... | ... |
| 105 pc S | 1890 | 85 | 29.4±6.5 | 650 | -55 | 31.1±6.6 | 1800 | 220 | 11.7±6.5 | 705 | -115 | 8.0±0.8 |
| 210 pc S | 370 | 595 | 1.6±0.2 | 720 | -75 | 7.8±0.5 | ... | ... | ... | ... | ... | ... |
| NGC 3227 | | | | | | | | | | | | |
| NUC | 965 | -125 | 4.09±0.56 | 520 | -35 | 20.04±0.9 | ... | ... | ... | ... | ... | ... |
| MCG-6-30-15 | | | | | | | | | | | | |
| NUC | 160 | -30 | 0.97±0.13 | 105 | -12 | 1.66±0.15 | 340 | -76 | 2.07±0.15 | 330 | -140 | 2.78±0.34 |
| | 670 | -277 | 1.21±0.30 | ... | ... | ... | 2090 | -340 | 4.33±1.00 | 1530 | -330 | 4.70±1.40 |
| NGC 3783 | | | | | | | | | | | | |
| NUC | 540 | -120 | 22.15±0.63 | 255 | -37 | 16.87±0.43 | 625 | -170 | 10.60±1.00 | 310 | -75 | 2.88±0.70 |
| | 1380 | -600 | 7.80±1.57 | ... | ... | ... | 1320 | -635 | 7.85±2.02 | 1080 | -320 | 7.69±2.37 |
| 270 pc N | ... | ... | ... | 310 | -39 | 2.19±0.17 | 650 | ... | ... | ... | ... | ... |
| 270 pc S | ... | ... | ... | 295 | 0.0 | 2.11±0.19 | 605 | ... | ... | ... | ... | ... |

^aTwo entries in a row gives the result of a two Gaussian fit to the line. Typical error in the Gaussian centroid is 20 km s⁻¹, but increases largely (50-100%) for low S/N lines

Table 5: FWHM and shifts from the centroid position (both in km/s), and fluxes (in units of 10^{-15} erg cm $^{-2}$ s $^{-1}$) for the NIR coronal lines measured in the nuclear and adjacent regions of the galaxy sample^a.

| Aperture (1) | [Si VI] | | | [Si VII] | | |
|-----------------|-------------|-------------------|----------------|-------------|-------------------|------------------|
| | FWHM (2) | ΔV (3) | Flux (4) | FWHM (5) | ΔV (6) | Flux (7) |
| Circinus | | | | | | |
| NUC | 125 | -37 | 37.6 \pm 1.7 | 100 | 18 | 53.0 \pm 0.4 |
| | 290 | -210 | 21.5 \pm 3.5 | 270 | -100 | 49.3 \pm 1.1 |
| 17 pc N | 145 | -60 | 6.8 \pm 2.0 | 100 | 20 | 1.9 \pm 0.2 |
| | 245 | -275 | 0.4 \pm 0.2 | 180 | -90 | 1.7 \pm 0.2 |
| 17 pc S | 140 | -45 | 12.2 \pm 2.7 | 100 | 28 | 2.8 \pm 0.2 |
| | ... | ... | ... | 170 | -85 | 4.40.6 |
| NGC 1068 | | | | | | |
| NUC | 950 | -185 | 421 \pm 90 | 330 | 0.0 | 117.3 \pm 13.8 |
| | ... | ... | ... | 730 | -250 | 131.0 \pm 30.0 |
| 45 pc N | 175 | -130 | 48.2 \pm 5.7 | 350 | 38 | 123.9 \pm 3.5 |
| | 710 | -180 | 259.5 \pm 13 | 710 | -270 | 89.8 \pm 6.9 |
| 90 pc N | 650 | -105 | 57.1 \pm 2.6 | 390 | 35 | 31.7 \pm 1.4 |
| | ... | ... | ... | 960 | -580 | 27.3 \pm 3.4 |
| 135 pc N | 790 | 47 | 9.4 \pm 3.1 | ... | ... | 26.0 \pm 2.4 |
| 45 pc S | 1090 | -38 | 164 \pm 36 | 290 | -60 | 34.3 \pm 3.0 |
| 90 pc S | 380 | 375 | 25.5 \pm 3.0 | ... | ... | ... |
| 135 pc S | 330 | 412 | 11.6 \pm 1.3 | 360 | 610 | 14.8 \pm 0.60 |
| NGC 3227 | | | | | | |
| NUC | 660 | -40 | 25.0 \pm 4.0 | ... | ... | ... |

^aA double entry in a row corresponds to the results from a two Gaussian fit to the line.

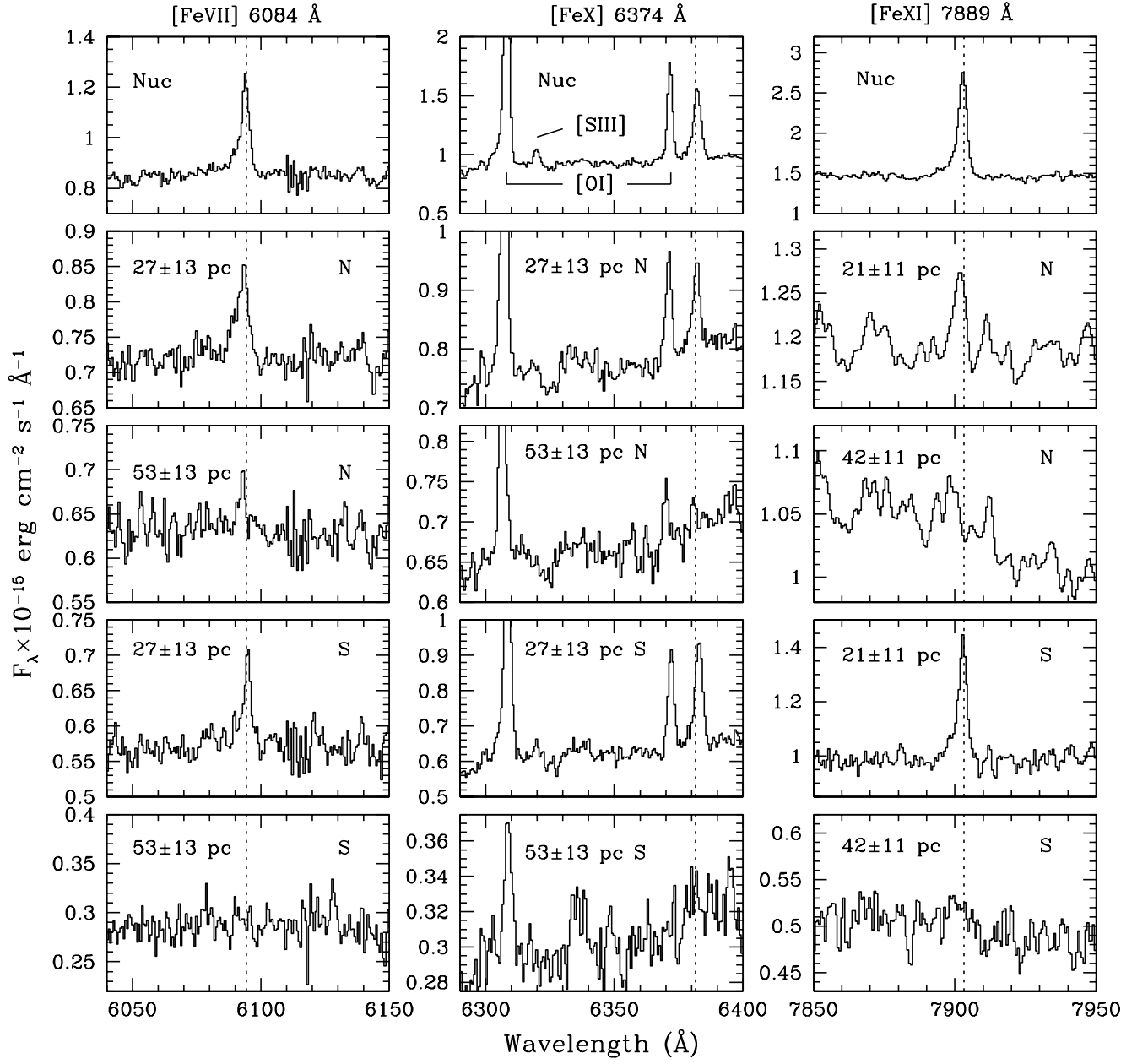


Fig. 1.— NTT spectra of Circinus along the spatial direction showing the extent of the [Fe VII] 6087 Å (left panels), [Fe X] 6374 Å (middle panels) and [Fe XI] 7889 Å (right panels). The spectra were extracted according to the aperture size D indicated in Table 2, and spatially correspond to a mean distance to the nucleus indicated in each box. The orientation of the slit is always north-south. The dot-line marks the systemic velocity at each of the three lines.

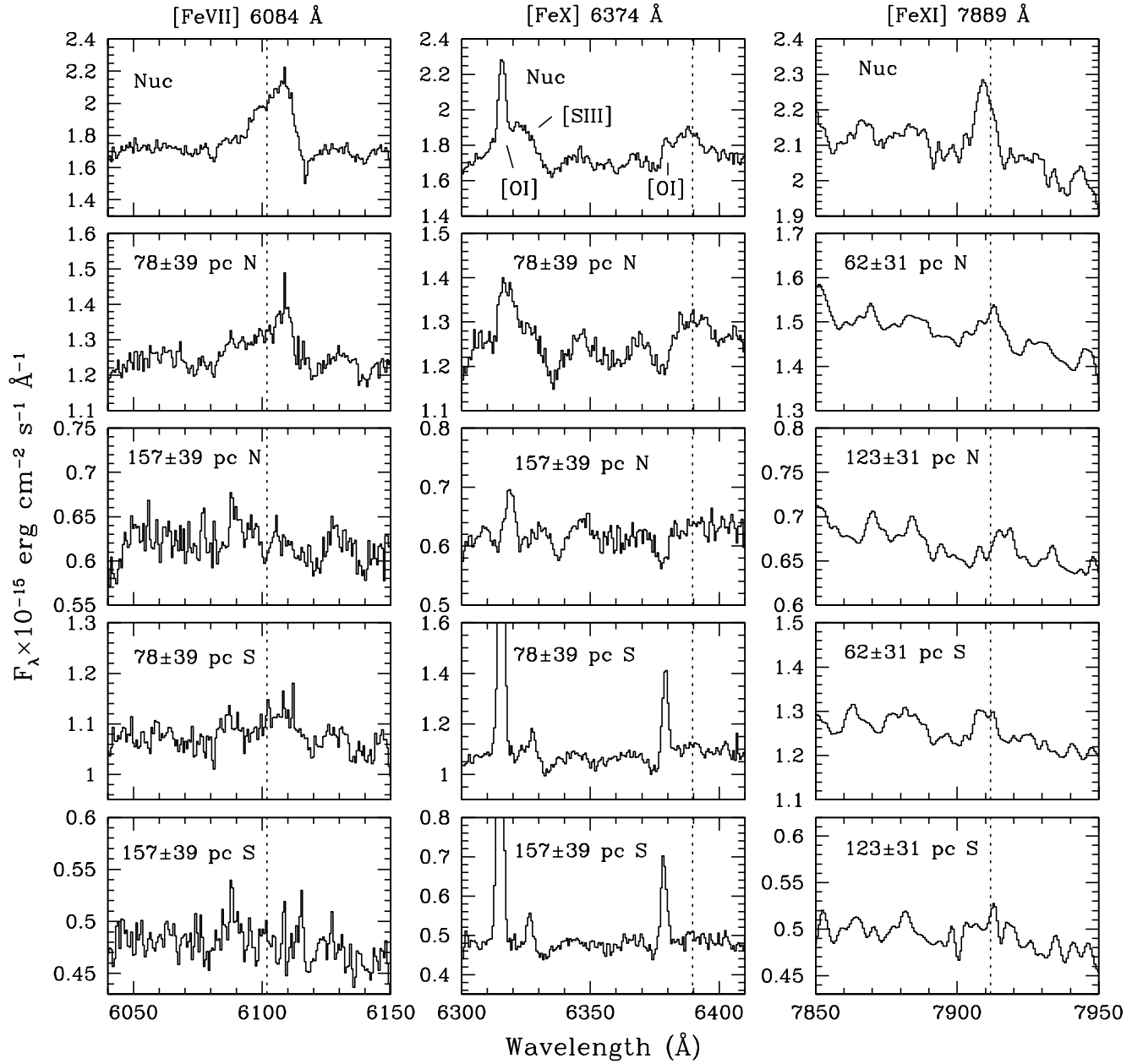


Fig. 2.— The same as Fig 1 for NGC 1386.

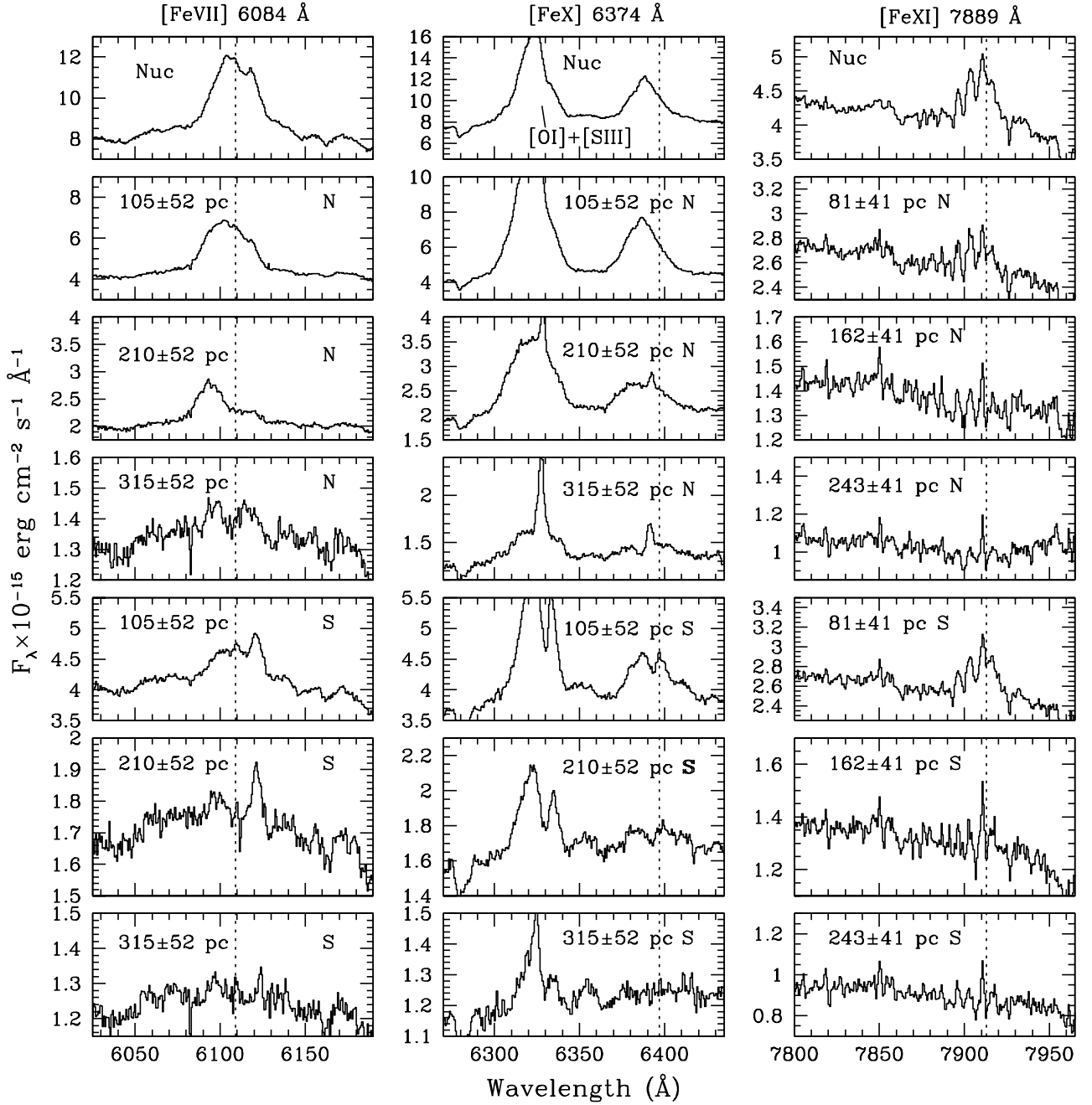


Fig. 3.— The same as Figure 1 for NGC 1068. In all positions, the presence of [Fe X] 6374 Å was determined after a consisting multigaussian fit to the region [O I]+[S III] – [O I]+[Fe X]. The strong line seen starting from 105 pc to the south, redwards of [O I] 6300, is presumably [S III] 6312 Å. Wrinkles on [Fe XI] line are telluric residuals.

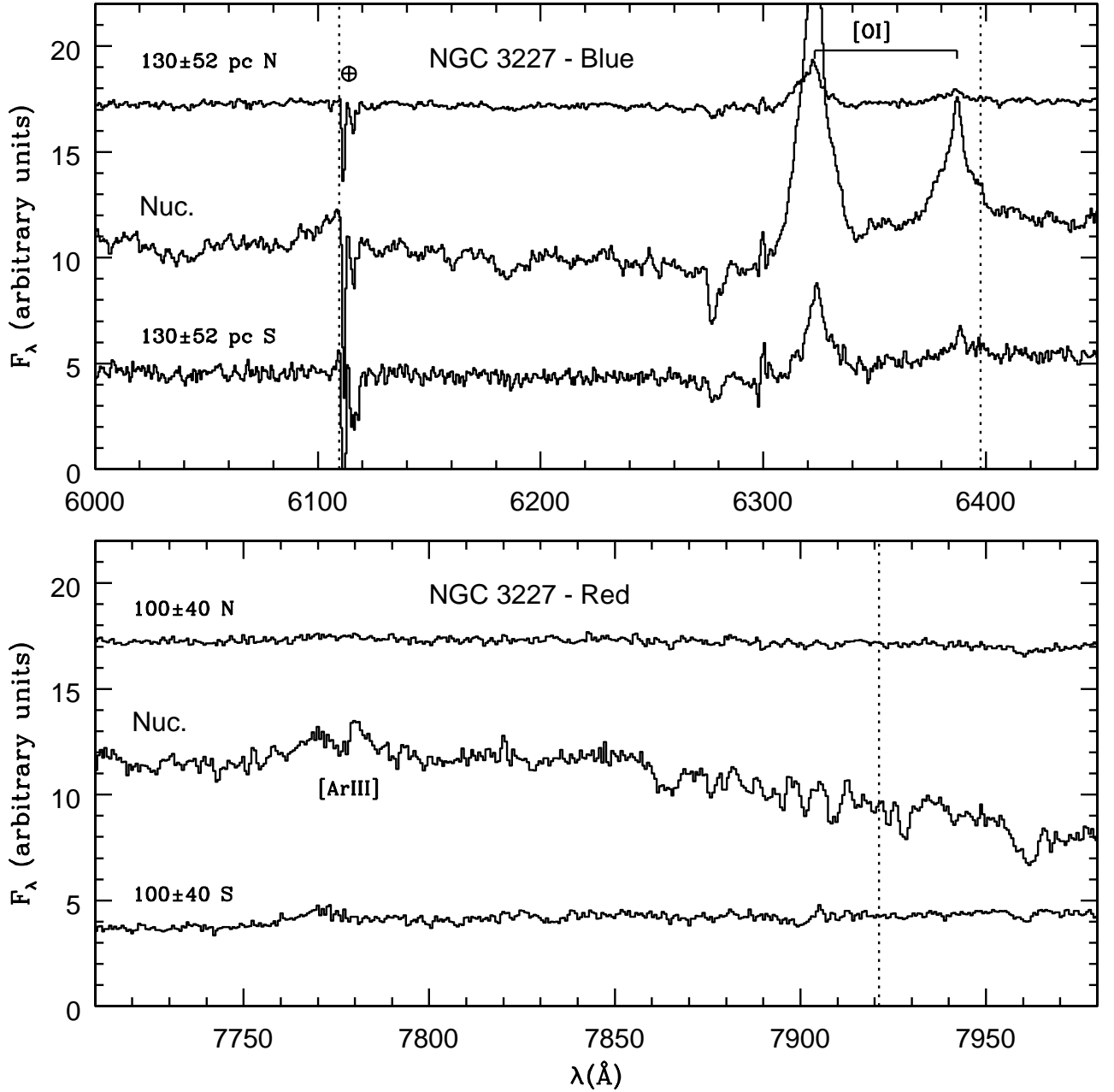


Fig. 4.— Extracted spectra for NGC 3227. The relative large size of the nuclear aperture used in this case is dictated by the number of spectra affected by scattered light by the broad line region - traced by $H\alpha$ in our spectra. This is to warrant the real spatial extension of coronal emission. The [Fe VII] profile is affected by sky residuals. This Seyfert type 1.5 is the only case in the sample lacking photons harder than 200 eV: [Fe XI] is not present, and most probably [Fe X] neither, which will fit with the lack of [Si VII] either (Fig. 9).

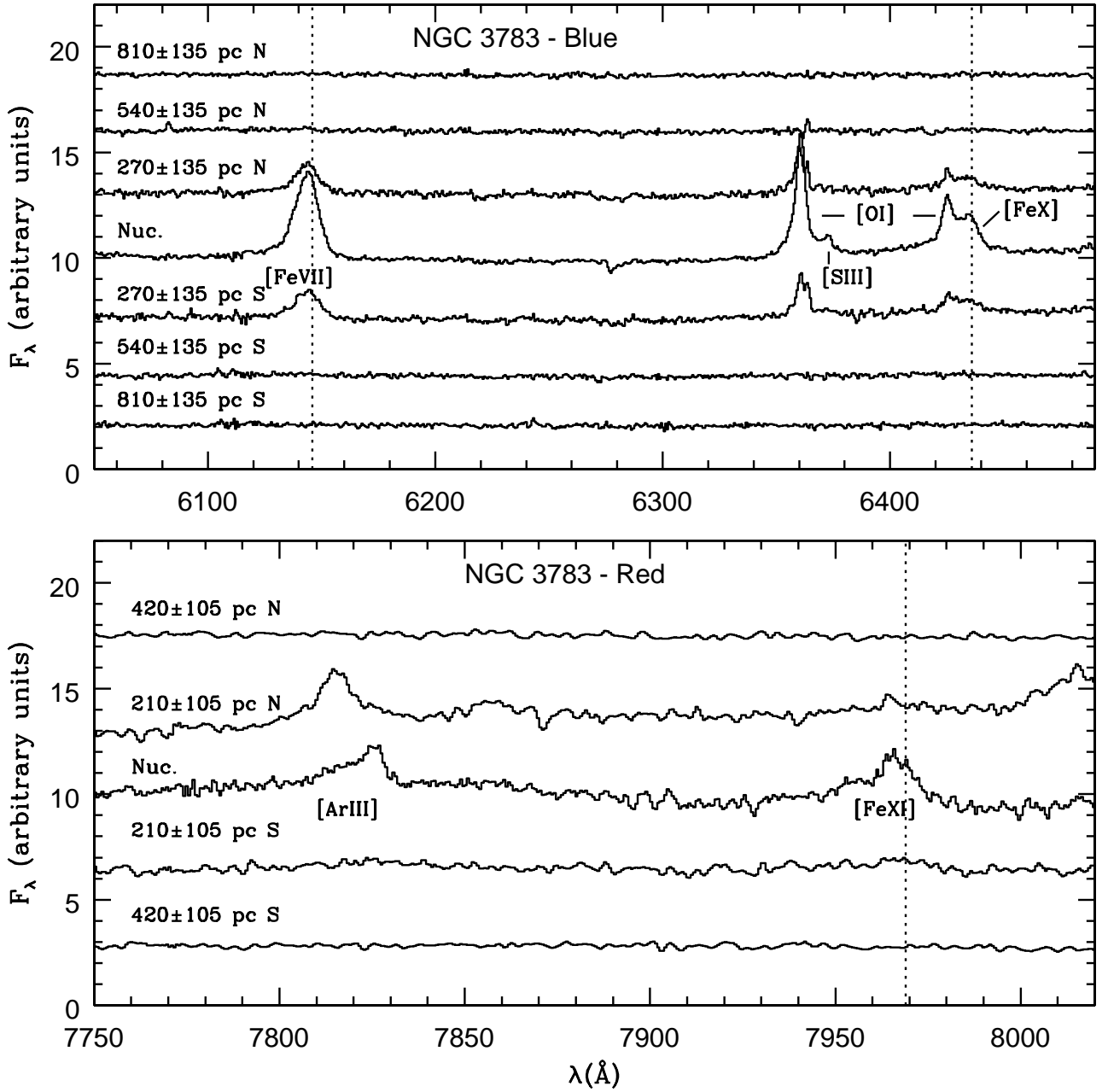


Fig. 5.— The same as Fig 4 for NGC 3783. As in NGC 3227, the relative large size of the nuclear aperture window was dictated by the number of spectra affected by scatter light from the broad line region - traced by H α in our spectra. This is to warrant the real spatial extension of coronal emission.

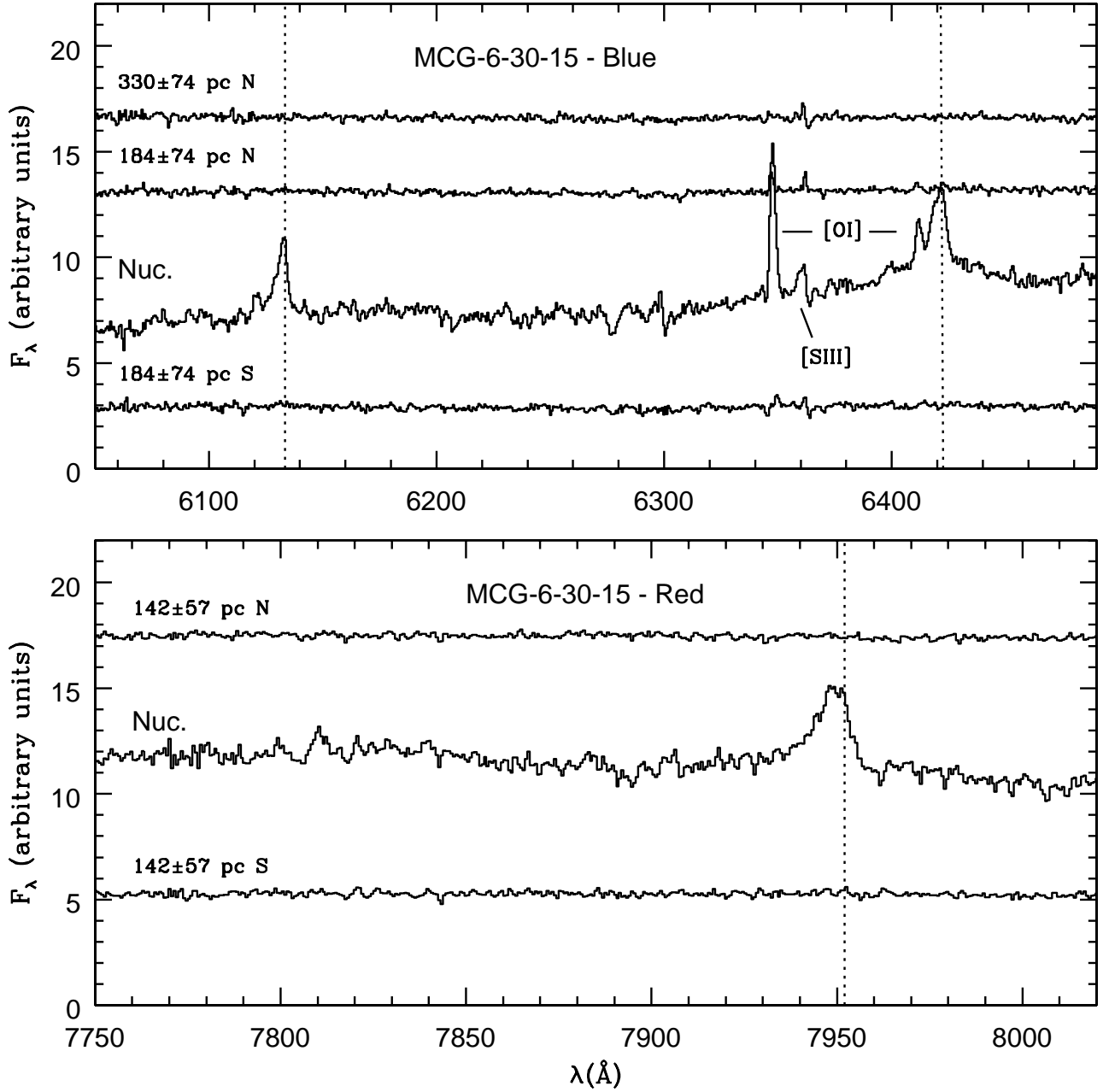


Fig. 6.— The same as Fig 4 for MCG-6-30-15.

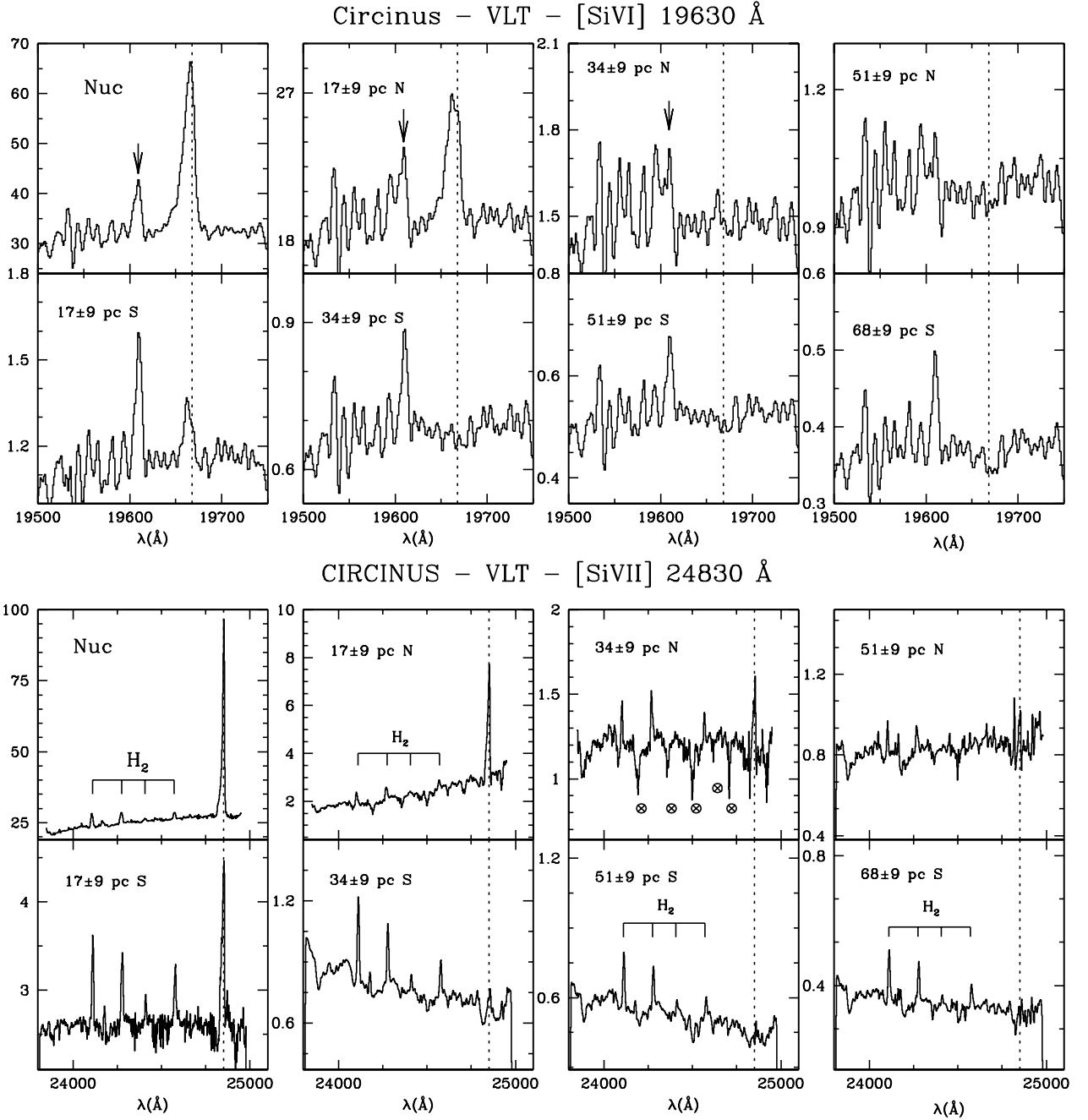


Fig. 7.— NIR VLT spectra of Circinus. Upper and lower panels show the spatial variation in the region around [Si VI] $1.693 \mu\text{m}$ and [Si VII] $2.47 \mu\text{m}$, respectively. In the upper panels the arrow indicate the expected position of H_2 $1.957 \mu\text{m}$. Expected positions of the $\text{Q}(0)\text{H}_2$ lines are marked in the bottom panels. The dotted line marks the position of the silicon line at the systemic velocity. The orientation of the slit is north-south. The Y-axis is in units of $\text{erg cm}^{-2} \text{s}^{-1} \text{\AA}^{-1}$.

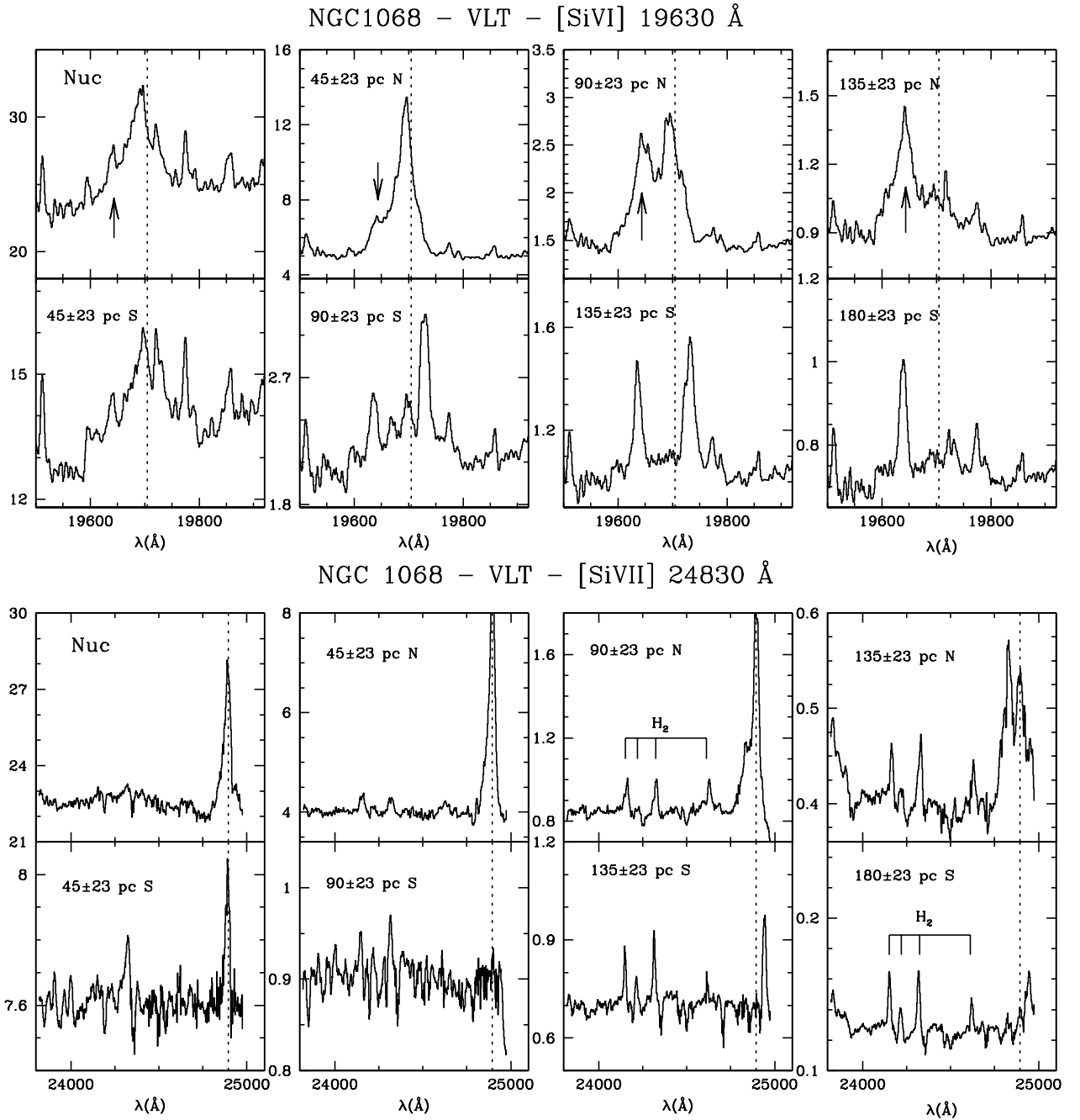
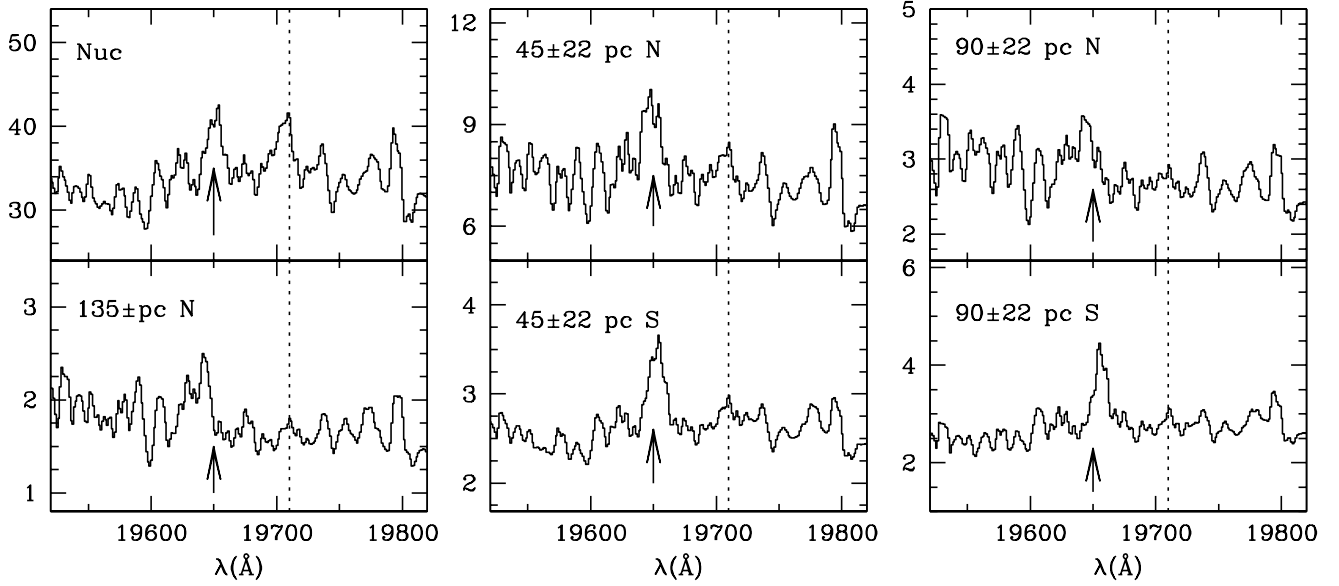


Fig. 8.— VLT/ISAAC spectra for NGC 1068. The notation is the same as in Figure 7. In NGC 1068 it is easily seen how the coronal gas moves faster than the more relaxed molecular gas: this can be appreciated by comparing, in particular, the shift of the [Si VI] line relative to that of the H_2 $1.957\mu\text{m}$.

NGC 3227 - VLT - [SiVI] 19630 Å



NGC 3227 - VLT - [SiVII] 24927 Å

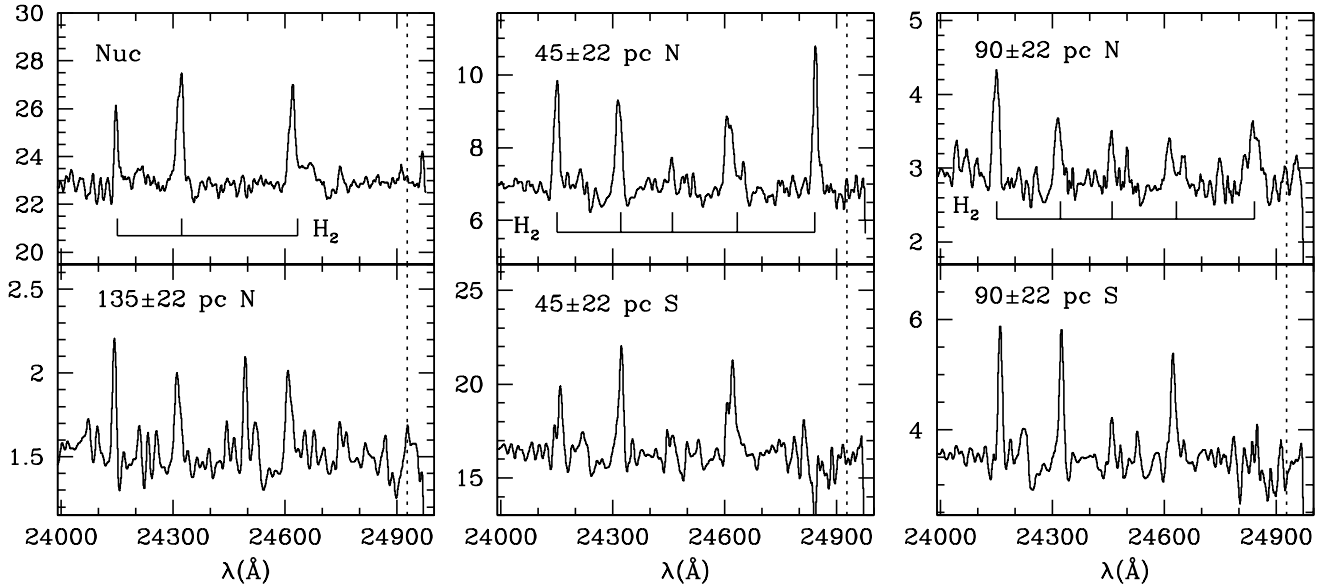


Fig. 9.— VLT/ISAAC spectra for NGC 3227. The notation is the same as in Figure 7. This galaxy lacks of [Si VII], which, as commented in Fig. 4 regarding to the absence of [Fe X] and [Fe XI] in this object, supports the hypothesis of a very soft ionizing radiation continuum.

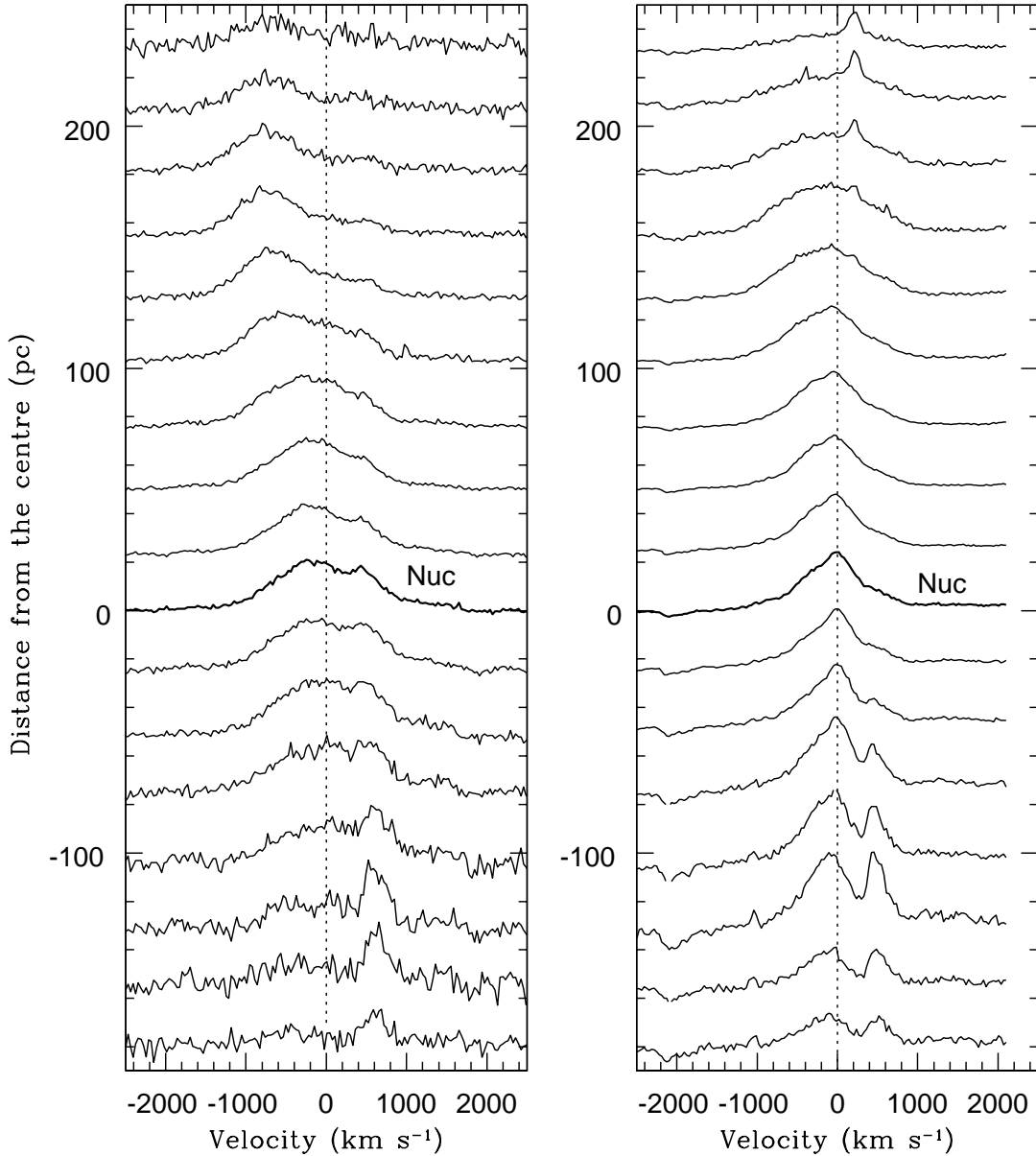


Fig. 10.— Pixel to pixel variation along the spatial direction of the emission line profiles of [Fe VII] 6087 Å (left panels) and [O I] 6300 Å (right panels), observed in NGC 1068. The dotted lines mark the position of the systemic velocity of the galaxy. The spectrum located at a distance of zero corresponds to the pixel containing the peak of light distribution. North is up and south is down. The spectra are spaced by 26 pc from each other and are plotted in an arbitrary intensity scale. [Fe VII] shows a double peak component, each peak moving blueward and redward from the systemic velocity at different spatial locations. We envisage a geometry by which this gas is moving in radial directions within a nuclear collimated wind, whose axis should be rather close to the plane of the sky. By comparison, [O I] is a slower gas. Its kinematics, nevertheless, is more difficult to interpret because of the satellite line [S III] 6312 Å, seen south of the nucleus, and presumably a [O I] narrow component seen to the north, also seen in [O I] 6363 Å in Fig. 3.

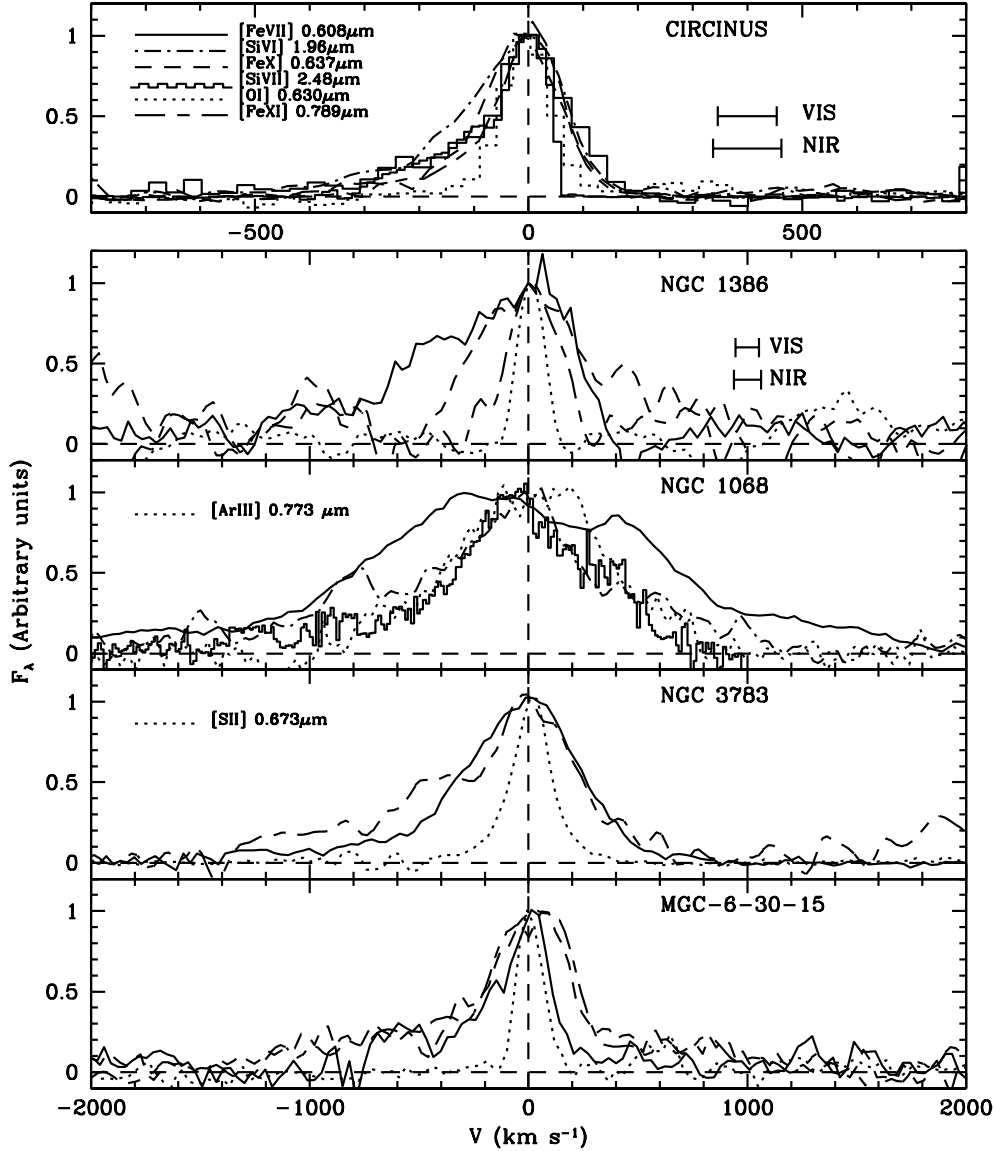


Fig. 11.— Comparison of the nuclear line profiles in velocity space for Circinus, NGC 1386, NGC 1068, NGC 3783 and MGC-6-30-15. Note that the velocity scale in Circinus is different from that in the other objects. In all cases, the low-ionization line profile (dotted line) is narrow - except in NGC 1068 - and symmetric whereas the coronal lines are significantly broader and asymmetric towards the blue. The error bars represent the FWHM of the instrumental profiles, measured from the arc lamp (optical) and sky-lines (NIR) respectively.

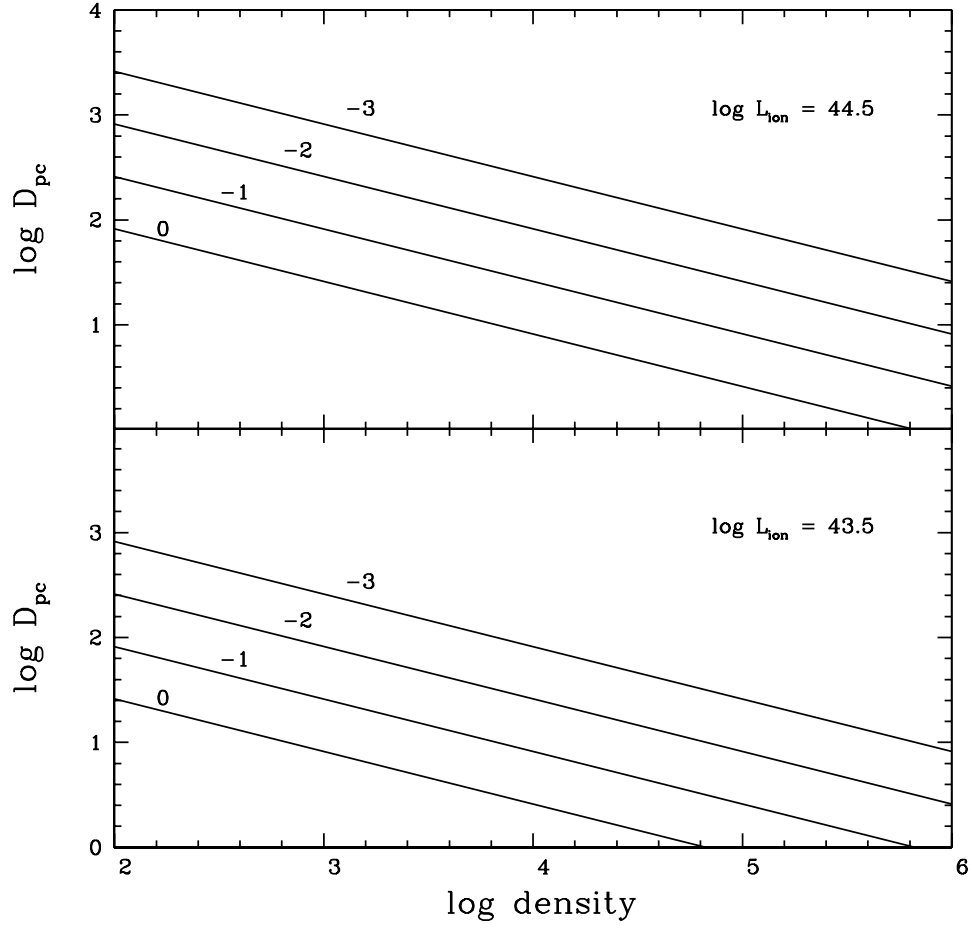


Fig. 12.— Relationship between D , the distance from the ionizing source (in parsecs) to the inner face of the cloud, and the gas density (in cm^{-3}) for $L_{\text{ion}} = 10^{44.5} \text{ erg s}^{-1}$ (upper panel) and $L_{\text{ion}} = 10^{43.5} \text{ erg s}^{-1}$ (lower panel). The curves are labelled according to the corresponding logarithm of U .

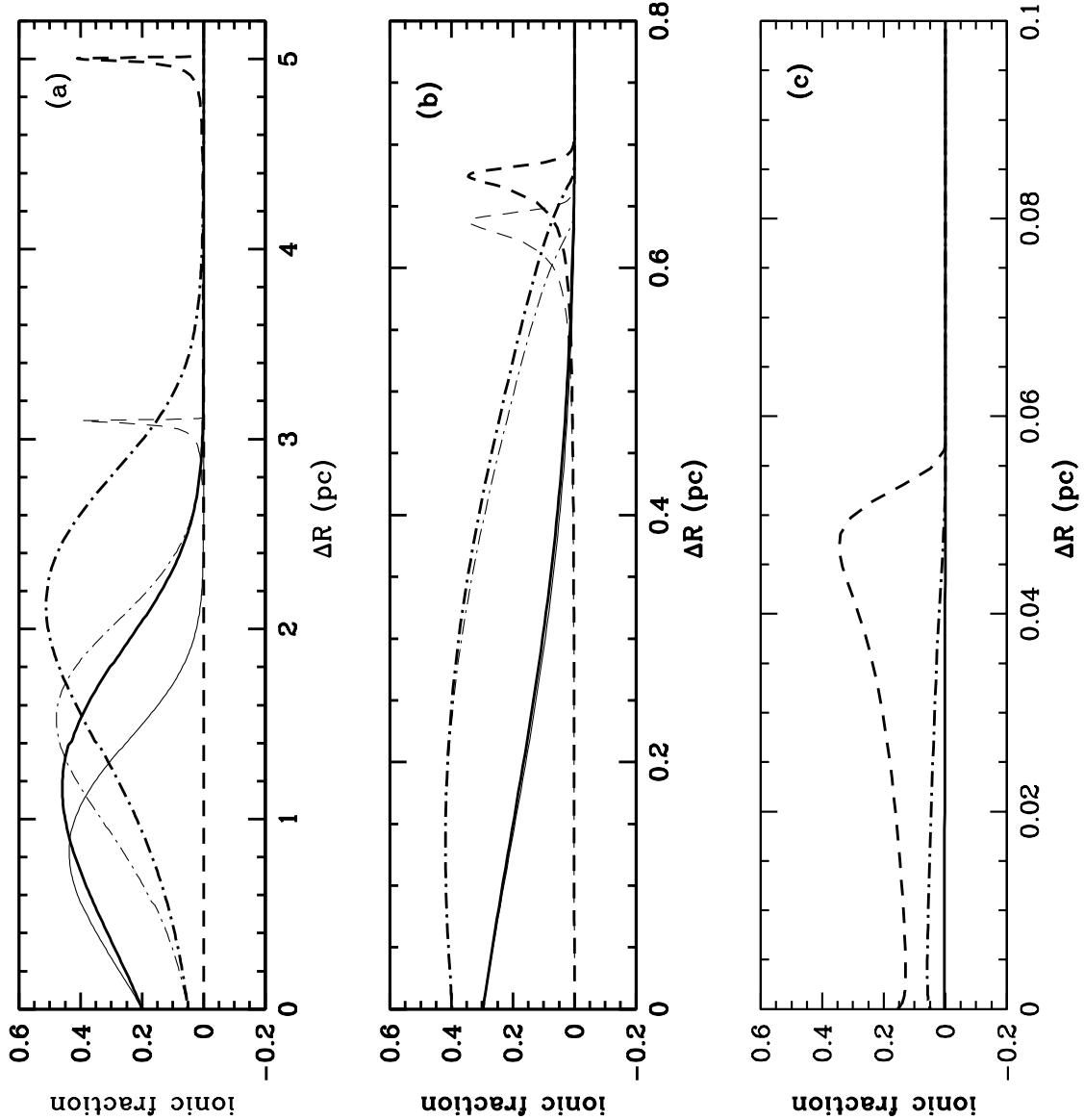


Fig. 13.— Ionic abundance for the Fe ions versus the geometrical depth of the cloud ΔR , for $L_{\text{ion}} = 10^{43.5} \text{ erg s}^{-1}$ (light lines) and $L_{\text{ion}} = 10^{44.5} \text{ erg s}^{-1}$ (thick lines): Fe^{+10} (solid lines), Fe^{+9} (dashed-dotted lines) and Fe^{+6} (dashed lines). Panels a, b, and c show the results for models with $U = 1, 0.1$ and 0.01 respectively, and density, $n_e = 10^4 \text{ cm}^{-3}$. In panel (c), the results corresponding to the two values of L_{ion} coincide and Fe^{+10} is not present in these clouds

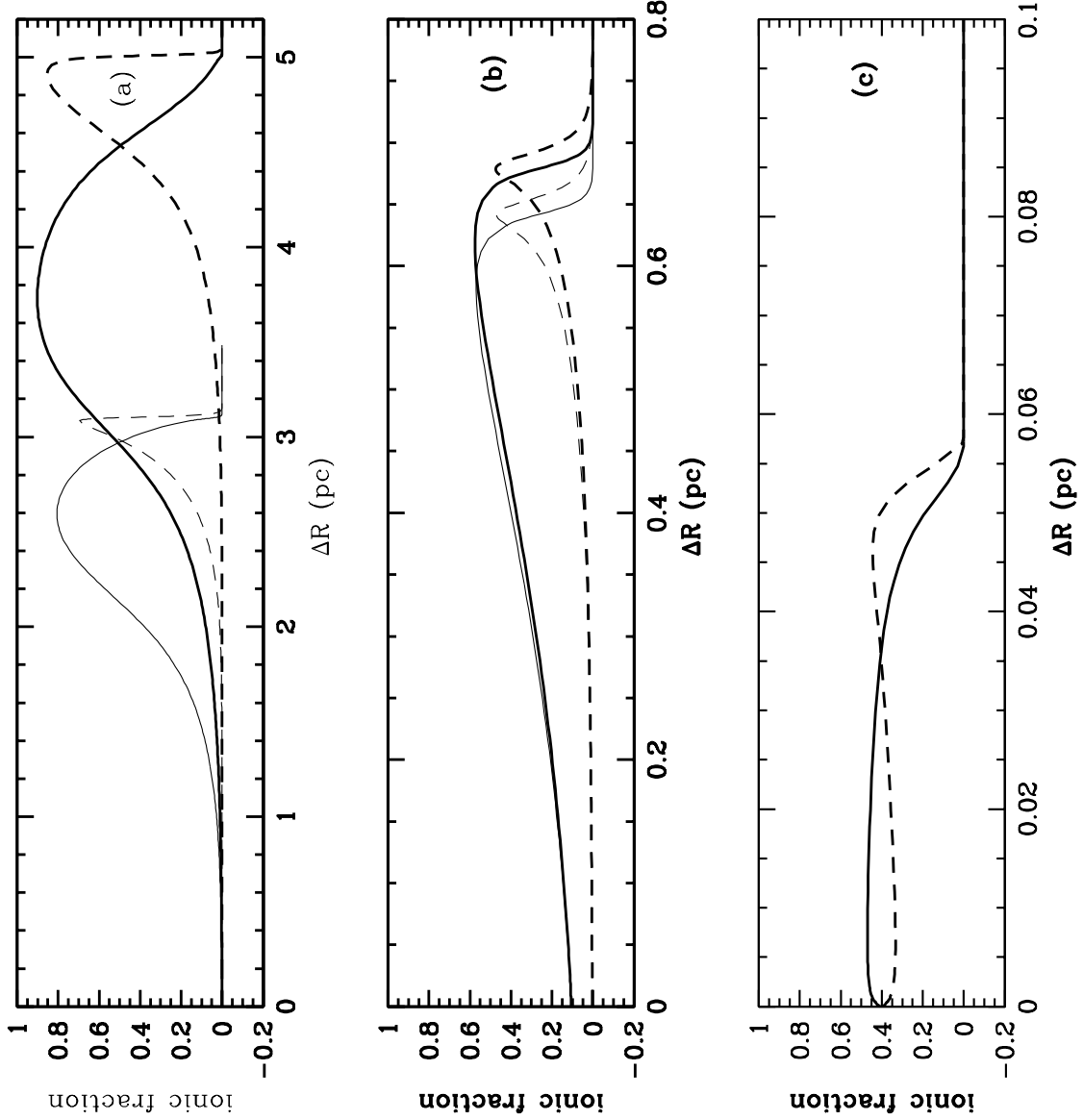


Fig. 14.— Ionic abundance of the Si ions versus the geometrical depth of the cloud ΔR , for $L_{\text{ion}} = 10^{43.5} \text{ erg s}^{-1}$ (light lines) and $L_{\text{ion}} = 10^{44.5} \text{ erg s}^{-1}$ (thick lines): Si^{+6} (solid lines), Si^{+5} (dashed lines). Panels a, b, and c show the results for models with $U=1, 0.1$ and 0.01 , respectively, and density, $n_e = 10^4 \text{ cm}^{-3}$. In panel (c), the results corresponding to the two values of L_{ion} coincide.

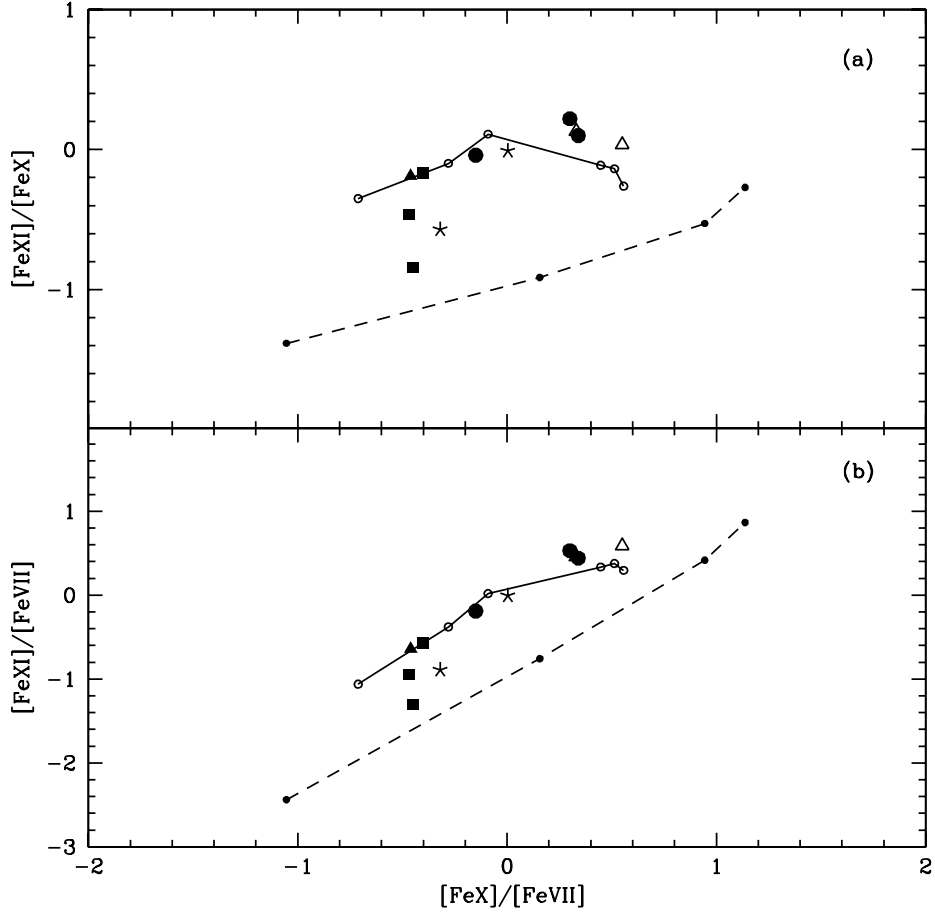


Fig. 15.— Observed Fe coronal line ratios for the nuclear and extended region measured in the AGN sample compared with predictions from pure photoionization models (dashed line, dots correspond to different values of U (-2, -1.5, -1, 0) for $n_e = 3 \times 10^3 \text{ cm}^{-3}$ and $L_{\text{ion}} = 10^{44.3} \text{ erg s}^{-1}$) and shock dominated models (solid line). For the later, the shock velocity varies from 300 km s^{-1} to 900 km s^{-1} , increasing from left to right. Most data points fall in the shock dominated region. Symbols correspond to different galaxies: filled circles, Circinus; filled triangles, NGC 1386; filled squares, NGC 1068; open triangles, MGC-6-30-15; and stars, NGC 3783.